Nano Research

ISSN 1998-0124 CN 11-5974/O4
https://doi.org/10.26599/NR.2026.94909255

Research Article

Engineering molecular-semiconductor interfaces via vacancy-triggered π–d coupling for H_2O_2 photosynthesis

Yihong Zhang[1,2,5], Yilong Yang[1,6](✉), Haishan Zhu[2,3], Yuen Zheng[1], Jiaqi Shen[2,3], Heju Guo[1], Longzhou Jin[2,3], Dan Liu[2,3], Silin Liu[1], Junshu Wu[4], Kaidong Xu[1], Yong Zhao[5], Songcan Wang[6](✉), Chunqiang Zhuang[2,3](✉)

[1] School of Materials and Chemical Engineering, Henan University of Urban Construction, Pingdingshan 467036, China

[2] Beijing Key Lab of Microstructure and Property of Advanced Materials, College of Material Science and Engineering, Beijing University of Technology, Beijing 100124, China

[3] Institute of Matter Science, Beijing University of Technology, Beijing 100124, China

[4] State Key Laboratory of Materials LoW–Carbon Recycling, College of Materials Science & Engineering, Beijing University of Technology, Beijing 100124, China

[5] Key Lab for Special Functional Materials of Ministry of Education, National & Local Joint Engineering Research Center for High-efficiency Display and Lighting Technology, School of Nano Science and Materials Engineering, Collaborative Innovation Center of Nano Functional Materials and Applications, Henan University, Kaifeng 475004, China

[6] State Key Laboratory of Flexible Electronics & School of Flexible Electronics, Northwestern Polytechnical University, 127 West Youyi Road, Xi'an 710072, China

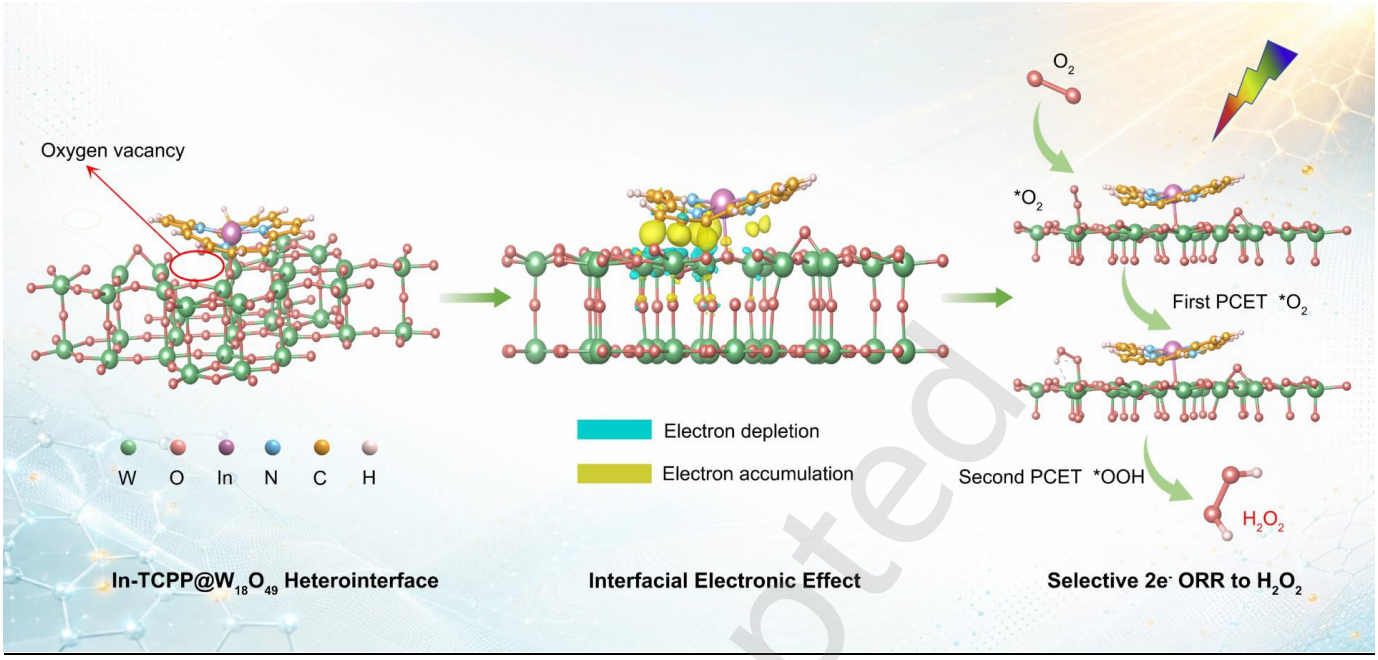
Nano Res., **Just Accepted Manuscript** • https://doi.org/10.26599/NR.2026.94909255
https://www.sciopen.com/journal/1998-0124 on Oct. 12, 2026

© The Authors(s)

Just Accepted

This is a "Just Accepted" manuscript, which has been examined by the peer-review process and has been accepted for publication. A "Just Accepted" manuscript is published online shortly after its acceptance,which is prior to technical editing and formatting and author proofing. Tsinghua University Press (TUP) provides "Just Accepted" as an optional and free service which allows authors to make their results available to the research community as soon as possible after acceptance. After a manuscript has been technically edited and formatted, and the page proofs have been corrected, it will be removed from the "Just Accepted" web site and published officially with volume and article number (e.g., *Nano Research*, **2025**, *18*, 94906990). Please note that technical editing may introduce minor changes to the manuscript text and/or graphics which may affect the content, and all legal disclaimers that apply to the journal pertain. In no event shall TUP be held responsible for errors or consequences arising from the use of any information contained in these "Just Accepted" manuscripts. To cite this anuscript please use its Digital Object Identifier (DOI®),which is identical for all formats of publication.

TABLE OF CONTENTS (TOC)



Oxygen-vacancy-enhanced π–d coupling enables interfacial charge transfer and selective O_2/OOH regulation for efficient H_2O_2 photosynthesis.

Just Accepted

Nano Research

Open Access

Research Article

Engineering molecular-semiconductor interfaces via vacancy-triggered π–d coupling for H_2O_2 photosynthesis

Yihong Zhang[1,2,5], Yilong Yang[1,6]✉, Haishan Zhu[2,3], Yuen Zheng[1], Jiaqi Shen[2,3], Heju Guo[1], Longzhou Jin[2,3], Dan Liu[2,3], Silin Liu[1], Junshu Wu[4], Kaidong Xu[1], Yong Zhao[5], Songcan Wang[6]✉, and Chunqiang Zhuang[2,3]✉

[1] *School of Materials and Chemical Engineering, Henan University of Urban Construction, Pingdingshan 467036, China*
[2] *Beijing Key Lab of Microstructure and Property of Advanced Materials, College of Material Science and Engineering, Beijing University of Technology, Beijing 100124, China*
[3] *Institute of Matter Science, Beijing University of Technology, Beijing 100124, China*
[4] *State Key Laboratory of Materials LoW–Carbon Recycling, College of Materials Science & Engineering, Beijing University of Technology, Beijing 100124, China*
[5] *Key Lab for Special Functional Materials of Ministry of Education, National & Local Joint Engineering Research Center for High-efficiency Display and Lighting Technology, School of Nano Science and Materials Engineering, Collaborative Innovation Center of Nano Functional Materials and Applications, Henan University, Kaifeng 475004, China*
[6] *State Key Laboratory of Flexible Electronics & School of Flexible Electronics, Northwestern Polytechnical University, 127 West Youyi Road, Xi'an 710072, China*

Received: 10 August 2026; **Revised:** 22 September 2026; **Accepted:** 12 October 2026

✉Address correspondence to Yilong Yang, ylyang@huuc.edu.cn; Songcan Wang, iamscwang@nwpu.edu.cn; Chunqiang Zhuang, chunqiang.zhuang@bjut.edu.cn

Cite this article: *Nano Research*, 2026, 19, 94909255 https://doi.org/10.26599/NR.2026.94909255

ABSTRACT: Photocatalytic H_2O_2 production is limited by slow interfacial charge transfer and poorly controlled adsorption of oxygen intermediates, which reduce the selectivity of the two-electron oxygen reduction reaction. We prepared an oxygen-vacancy-rich In-TCPP@$W_{18}O_{49}$ heterointerface to investigate the role of π–d orbital coupling in oxygen reduction. Experiments and calculations show that oxygen vacancies enhance hybridization between the π states of In-TCPP and the W 5d states of $W_{18}O_{49}$. This interaction promotes interfacial charge redistribution and modifies the local electronic structure of surface W sites. The resulting electronic changes facilitate interfacial electron transfer and regulate the adsorption energies of $*O_2$ and *OOH intermediates, favoring a selective two-electron pathway for H_2O_2 formation. The optimized In-TCPP@$W_{18}O_{49}$ produces H_2O_2 at 1045 μmol g^{-1} h^{-1} in pure water under ambient air, 10.7 times higher than $W_{18}O_{49}$, with a solar-to-chemical conversion efficiency of 1.66 %. These findings indicate how oxygen-vacancy-enhanced π–d coupling may influence oxygen reduction and provide insights into designing selective solar-driven oxygen reduction photocatalysts.

KEYWORDS: photocatalytic H_2O_2 production; oxygen reduction reaction; oxygen vacancies; interfacial π–d coupling; orbital-level interface engineering; organic–inorganic hybrid interface.

1 Introduction

Hydrogen peroxide (H_2O_2) is an important oxidizing chemical used in environmental treatment, chemical synthesis, and energy-related applications [1–3]. Its commercial production is currently dominated by the anthraquinone process, which involves considerable energy consumption and complex processing steps [4, 5]. Solar-driven photocatalytic oxygen reduction provides an alternative route for H_2O_2 synthesis under mild conditions [6, 7]. However, competing reduction pathways make it difficult to achieve both high production efficiency and high selectivity.

Selective H_2O_2 formation through photocatalytic ORR depends on interfacial charge transfer and the adsorption energetics of oxygen intermediates [8, 9]. Limited extraction and transport of photogenerated electrons lead to charge recombination and reduce the electrons available for O_2 activation [10–12]. The adsorption configuration and reduction barriers of oxygen intermediates determine whether O_2 undergoes two- or four-electron reduction. Appropriate stabilization of OOH promotes H_2O_2 formation through the two-electron pathway, whereas excessively strong adsorption may induce O–O bond cleavage and further reduction reactions [13–16]. Effective photocatalysts should therefore facilitate electron transfer while maintaining suitable interactions with oxygen intermediates.

Defect engineering and heterojunction construction have been widely used to regulate the electronic structures of photocatalysts [17–20]. For example, asymmetric oxygen vacancies in $ZnGa_2O_4$ were reported to tune defect states and weaken the excessive intermediate adsorption commonly associated with conventional oxygen vacancies [21]. This regulation improves oxygen activation and reactive oxygen species generation. In CdS/NiPc heterojunctions, orbital hybridization induced by interfacial chemical bonds provides directional charge-transfer pathways and modifies oxygen-intermediate adsorption, favoring selective H_2O_2 production [22].

Just Accepted

Recently, porphyrin-based molecular frameworks have attracted considerable attention for photocatalytic H_2O_2 production owing to their well-defined π-conjugated structures and strong light-harvesting capability [23–25]. It has been demonstrated that porphyrin-based supramolecular photocatalysts enable ultrafast electron transfer and facilitate •OOH generation, revealing the unique advantages of delocalized π-electronic structures for photocatalytic oxygen reduction [26]. Therefore, if such oxygen-vacancy-rich transition metal oxides are coupled with porphyrin-based molecular photocatalysts, the resulting interfacial π–d coupling can directly reconstruct local electronic states and modulate oxygen intermediate energetics, which can simultaneously optimize interfacial electron transfer kinetics and reaction pathway selectivity for efficient photocatalytic H_2O_2 production.

Herein, we constructed an oxygen-vacancy-rich In-TCPP@$W_{18}O_{49}$ composite photocatalytic system to elucidate the mechanism by which oxygen-vacancy-induced interfacial π–d coupling regulates selective photocatalytic oxygen reduction. $W_{18}O_{49}$ was selected as the inorganic component because of its abundant oxygen vacancies and highly tunable W 5d electronic states, which provide an ideal platform for defect-mediated electronic regulation. In-TCPP, featuring an extended porphyrinic π-conjugated skeleton, offers excellent visible-light response and favorable molecular characteristics for oxygen activation. The intimate interfacial coupling between these two components creates a π–d electronic coupling interface, enabling synergistic regulation of interfacial charge transfer kinetics and oxygen reduction reaction chemistry. The oxygen vacancies enhance electronic coupling between porphyrinic π states and W 5d orbitals, thereby inducing accompanied by interfacial charge redistribution and changes in the local electronic structure. confirming intimate interfacial contact The interfacial π–d interaction promotes photogenerated electron transfer and adjusts the adsorption behavior of oxygen intermediates. These effects favor selective H_2O_2 formation through a stepwise two-electron oxygen reduction pathway. Accordingly, the optimized In-TCPP@$W_{18}O_{49}$ achieves a high H_2O_2 production rate of 1045 μmol g^{-1} h^{-1} under pure water, ambient air, and without any sacrificial agent. This work provides evidence for the contribution of oxygen-vacancy-induced interfacial π–d coupling to oxygen reduction selectivity, providing mechanistic insights for orbital-level interfacial engineering toward selective solar-to-chemical conversion.

2 Experimental

2.1. Synthesis of $W_{18}O_{49}$

WCl_6 (0.625 mmol) was added to 50 mL of ethanol under stirring. The mixture was transferred into a 100 mL autoclave and maintained at 180 °C for 24 h. The recovered solid was washed with deionized water followed by ethanol and dried overnight at 60 °C. Annealing the dried powder at 300 °C for 1 h under N_2 yielded oxygen-vacancy-rich $W_{18}O_{49}$. The $W_{18}O_{49}$ powder was calcined in air at 650 °C for 4 h to obtain the WO_3 control.

2.2. Synthesis of In-TCPP

$In(NO_3)_3 \cdot xH_2O$ (30 mg, 0.10 mmol) and H_2TCPP (32.0 mg, 0.04 mmol) were dispersed in DMF (10.0 mL). The suspension was sonicated for 10 min to remove possible air bubbles and maintained in an oil bath at 130 °C for 5 h. The purple solid was separated by centrifugation, washed three times each with DMF and ethanol, and vacuum-dried at 60 °C for 12 h to obtain In-TCPP crystals.

2.3. Synthesis of In-TCPP@$W_{18}O_{49}$

In-TCPP@$W_{18}O_{49}$ was prepared by adding pre-synthesized $W_{18}O_{49}$ (10, 20, 30, 40, or 50 mg) to 10.0 mL of DMF containing $In(NO_3)3 \cdot xH_2O$ (30 mg, 0.10 mmol) and H_2TCPP (32.0 mg, 0.04 mmol). The amount of W18O49 was varied to adjust the nominal In-TCPP loading. After sonication for 10 min to remove air bubbles, the mixture was maintained in an oil bath at 130 °C for 5 h. The solid was recovered by centrifugation, washed three times each with DMF and ethanol, and vacuum-dried at 60 °C for 12 h. The obtained samples were denoted as In-TCPP@$W_{18}O_{49}$-10, In-TCPP@$W_{18}O_{49}$-20, In-TCPP@$W_{18}O_{49}$-30, In-TCPP@$W_{18}O_{49}$-40, and In-TCPP@$W_{18}O_{49}$-50, where the numerical suffix indicates the initial mass of $W_{18}O_{49}$ added in milligrams. The suffix does not represent the measured In-TCPP mass fraction. All samples in this series were prepared using a reaction time of 5 h.

3 Results and discussion

3.1. Construction and Structural Characterization of the In-TCPP@$W_{18}O_{49}$

As illustrated in Figure 1a, oxygen-vacancy-rich $W_{18}O_{49}$ nanorods were first prepared via a solvothermal method, followed by the in situ growth of In-TCPP on their surface to construct a tightly coupled organic–inorganic hybrid interface. The representative In-TCPP@$W_{18}O_{49}$ hybrid discussed throughout this work corresponds to the optimized composition obtained after systematic tuning of the synthetic parameters. X-ray diffraction (XRD) and transmission electron microscopy (TEM) were used to characterize the phase composition and morphology of the samples. The XRD pattern of the hybrid retains the main reflections of $W_{18}O_{49}$, while the characteristic features of In-TCPP are also observed, supporting the formation of the hybrid structure. Pristine $W_{18}O_{49}$ shows diffraction peaks assigned to monoclinic $W_{18}O_{49}$, with the (010) and (020) reflections showing relatively higher intensities (Figure 1b) [27, 28]. In contrast, In-TCPP displays a distinct diffraction peak assignable to the (021) plane, originating from its ordered molecular stacking structure [29]. Importantly, all these characteristic reflections are well retained in the In-TCPP@$W_{18}O_{49}$ composite, indicating the coexistence of both crystalline components after hybridization. Subtle variations in peak profiles can be observed after hybridization, suggesting possible interfacial interactions between In-TCPP and $W_{18}O_{49}$ at the structural level. FTIR spectra (Figure S1) further support the successful integration of In-TCPP with $W_{18}O_{49}$. Pristine $W_{18}O_{49}$ exhibits characteristic W=O/W-O-W vibrational features mainly in the low-wavenumber region around 800-900 cm^{-1}, consistent with the tungsten oxide framework. In-TCPP displays multiple absorption bands in the 1000-1700 cm^{-1} region, which can be assigned to porphyrinic skeleton vibrations, including C-N stretching, coupled C=C/C=N framework vibrations, and carboxylate-related modes [30–32]. The FTIR spectrum of In-TCPP@$W_{18}O_{49}$ contains bands from both In-TCPP and $W_{18}O_{49}$, supporting the presence of the two components in the hybrid. Small shifts and changes in relative intensities occur in the W-O region and in bands associated with the porphyrin structure. These differences suggest that the local bonding environments

Just Accepted

are altered after hybridization and may arise from interactions at the In-TCPP@$W_{18}O_{49}$ interface.

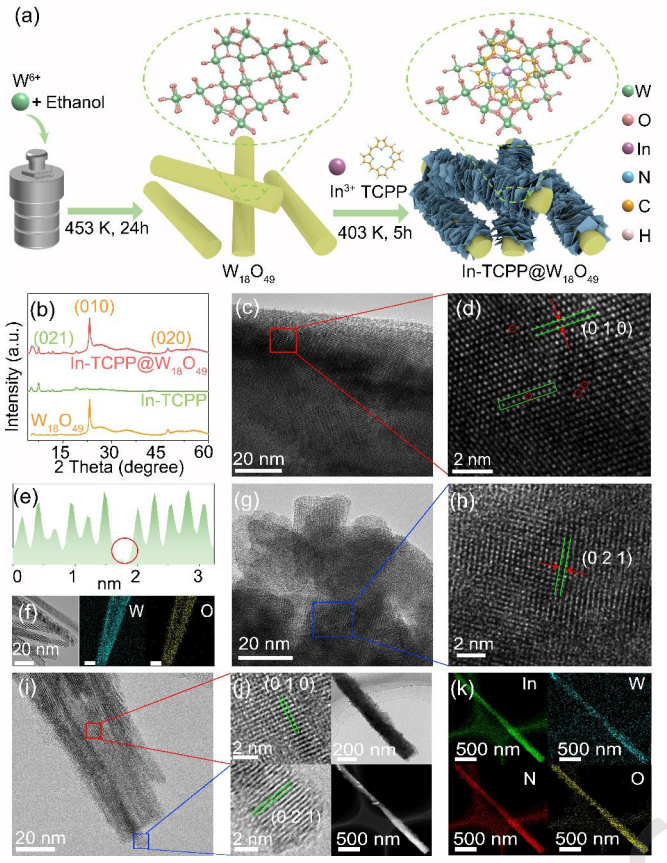


Figure 1. (a) Schematic representation of the synthesis of In-TCPP@$W_{18}O_{49}$. (b) XRD patterns of W18O49, In-TCPP, and In-TCPP@$W_{18}O_{49}$. (c) TEM image, (d) HR-TEM image and I corresponding line intensity profile of pristine $W_{18}O_{49}$. (f) STEM-EDS elemental mapping of $W_{18}O_{49}$. (g, h) TEM and HRTEM images of In-TCPP. (I, j) TEM, HR-TEM and HAADF images of In-TCPP@$W_{18}O_{49}$ at different magnifications. (k) STEM-EDS elemental mapping of In, N, W, and O.

TEM images of pristine $W_{18}O_{49}$ (Figure 1c) show nanorods with relatively smooth surfaces. The HRTEM image (Figure 1d) contains clear lattice fringes indexed to the (010) plane of monoclinic $W_{18}O_{49}$, indicating good crystallinity. The red-circled areas show local lattice distortion and interruptions in fringe continuity. The corresponding line intensity profile (Figure 1e) exhibits pronounced attenuation in periodic contrast, indicating the destruction of local lattice periodicity and reflecting structural disorder associated with oxygen defects. STEM-EDS mapping (Figure 1f) further confirms the homogeneous distribution of W and O throughout the uniformly dispersed nanorod framework. Figure 1g, h reveal that pristine In-TCPP possesses well-defined nanosheet-like morphology with discernible lattice fringes indexed to the (021) plane, indicating a high degree of molecular crystalline order. Furthermore, STEM-EDS elemental mapping of pristine In-TCPP (Figure S2) reveals the homogeneous distribution of In, N, C, and O throughout the nanosheet framework, further confirming the uniform molecular composition of the porphyrinic structure. After hybridization, TEM imaging (Figure 1i) shows that the nanorod morphology is well preserved, while a roughened outer layer appears on the nanorod surface, indicating the successful deposition of In-TCPP. HRTEM analysis (Figure 1j) reveals distinct lattice fringes originating from both $W_{18}O_{49}$ (010) and In-TCPP (021), indicating close interfacial contact between the two components. Furthermore, STEM-EDS elemental mapping (Figure 1k) demonstrates the uniform spatial distribution of In, N, W, and O throughout the hybrid architecture, supporting the successful assembly of In-TCPP onto W18O49.

3.2. Oxygen-Vacancy-Mediated Interfacial Electronic Coupling

To examine the electronic interaction formed at the In-TCPP@$W_{18}O_{49}$ interface, high-resolution XPS spectra were analyzed. The W 4f spectrum of $W_{18}O_{49}$ can be deconvoluted into a W^{6+} doublet at approximately 35.8 and 37.9 eV, together with lower-binding-energy W^{5+} components associated with the oxygen-deficient tungsten oxide structure (Figure 2a) [33–35]. After coupling with In-TCPP, the W 4f components shift slightly toward higher binding energy, indicating a decrease in electron density around the W sites. In contrast, the N 1s components of In-TCPP@$W_{18}O_{49}$ shift toward lower binding energy relative to those of In-TCPP (Figure 2b). The peaks at approximately 398.0 and 400.0 eV are assigned to iminic nitrogen (−C=N−) and pyrrolic nitrogen (−C−N−), respectively [36–38]. The opposite W 4f and N 1s shifts are consistent with interfacial electron redistribution from the tungsten oxide component toward the porphyrinic unit. The O 1s spectrum contains lattice oxygen, defect-associated oxygen, and surface-adsorbed oxygen components at approximately 530.3, 531.5, and 532.5 eV, respectively (Figure 2c) [39, 40]. Changes in the defect-associated component after hybridization further indicate that the local environment around surface oxygen-deficient sites is perturbed by interface formation. The XPS survey spectrum and the In_{3d} and C_{1s} spectra in Figure S3 confirm the presence of the expected surface elements in the composite.

The XPS survey spectrum and supplementary high-resolution spectra of In 3d and C 1s (Figure S3) further confirm the successful incorporation of In-TCPP and the surface elemental composition of the composite system [37, 41]. These results also provide additional support for the interfacial electronic interaction between In-TCPP and W18O49. ICP-OES analysis of the optimized In-TCPP@$W_{18}O_{49}$ sample gave W and In contents of 67.65 and 16.32 wt%, respectively. Assuming that the dry sample consists solely of stoichiometric $W_{18}O_{49}$ and In-TCPP, the W content corresponds to an estimated In-TCPP mass fraction of 16.32 wt%. The calculation and its assumptions are provided in the Supporting Information.

Just Accepted

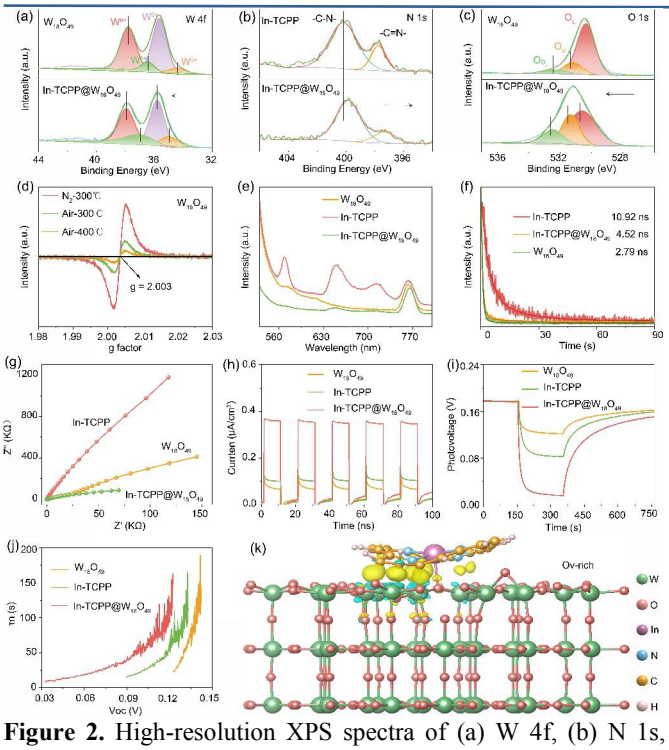


Figure 2. High-resolution XPS spectra of (a) W 4f, (b) N 1s, and (c) O 1s for the indicated samples. (d) EPR spectra of $W_{18}O_{49}$ samples treated under N_2 at 300 °C and in air at 300 and 400 °C. (e) Steady-state photoluminescence (PL) spectra and (f) time-resolved photoluminescence (TRPL) decay curves of $W_{18}O_{49}$, In-TCPP, and In-TCPP@$W_{18}O_{49}$. (g) Electrochemical impedance spectroscopy (EIS) Nyquist plots, (h) transient photocurrent responses, (i) open-circuit voltage decay (OCVD) curves, and (j) corresponding electron lifetimes of the indicated samples. (k) Charge density difference at the oxygen-vacancy-rich In-TCPP@$W_{18}O_{49}$ interface. Yellow and cyan regions indicate electron accumulation and depletion, respectively.

Electron paramagnetic resonance (EPR) was used to compare $W_{18}O_{49}$ samples treated under N_2 at 300 °C and in air at 300 and 400 °C. The signal at g = 2.003 is assigned to trapped electrons associated with oxygen-vacancy defects [42–44]. It is strongest for the N_2–300 °C sample and decreases after treatment in air at 300 and 400 °C (Figure 2d). The normalized double-integrated intensities are 1.00, 0.27, and 0.10, respectively (Figure S4a), providing a semiquantitative comparison of vacancy-associated paramagnetic centers rather than absolute oxygen-vacancy concentrations. The XRD patterns of all three samples retain the characteristic reflections of $W_{18}O_{49}$ (Figure S4b), indicating that the decrease in the EPR signal is not accompanied by a detectable change in the principal crystalline phase.

Photoluminescence (PL) spectra were further recorded to evaluate the charge-carrier recombination behavior (Figure 2e). In-TCPP exhibits multiple emission features in the visible region, which are associated with the characteristic vibronic transitions of the porphyrinic framework. After coupling with $W_{18}O_{49}$, the steady-state PL intensity of In-TCPP is reduced, consistent with suppressed radiative emission. TRPL measurements (Figure 2f) give average lifetimes of 10.92 ns for In-TCPP and 4.52 ns for In-TCPP@$W_{18}O_{49}$. A shorter PL lifetime may result from either interfacial charge transfer or nonradiative recombination. In this system, the enhanced photocurrent response and reduced impedance of the hybrid support more efficient interfacial charge transfer [45, 46]. The EIS spectrum (Figure 2g) shows the smallest Nyquist semicircle for In-TCPP@$W_{18}O_{49}$, suggesting lower interfacial charge-transfer resistance. The hybrid also exhibits the highest transient photocurrent response (Figure 2h), indicating improved separation and transport of photogenerated carriers. OCVD measurements were performed to evaluate charge decay after light interruption. In-TCPP@$W_{18}O_{49}$ shows the slowest photovoltage decay (Figure 2i) and a longer calculated electron lifetime (Figure 2j) than the individual components. TRPL and OCVD reflect different aspects of carrier dynamics: TRPL describes excited-state decay on the nanosecond timescale, whereas OCVD monitors charge loss after illumination. Together, these results suggest more efficient interfacial charge transfer and reduced loss of separated carriers.

Differential charge-density calculations were used to visualize the interfacial redistribution suggested by XPS. At the oxygen-vacancy-rich interface, electron depletion is concentrated around W sites adjacent to the vacancies, whereas electron accumulation extends over the porphyrinic macrocycle (Figure 2k). This spatial distribution agrees with the higher-binding-energy shift of W_{4f} and the lower-binding-energy shift of N_{1s}, linking the calculated redistribution to the experimentally observed changes in the local electronic environments of W and N.

The role of oxygen vacancies was examined by comparing interfaces with and without additional surface oxygen vacancies (Figure S5). Under the same isosurface criterion, the vacancy-rich model shows more pronounced electron accumulation and depletion around the interfacial W sites and the porphyrinic unit. The comparison indicates that additional surface oxygen vacancies amplify the interfacial polarization. These results locate the charge redistribution inferred from XPS but do not, by themselves, quantify the strength of π–d hybridization; its orbital origin is examined below using PDOS and pCOHP analyses.

3.3. Electronic-State and Optical Characterization

VB-XPS and optical spectroscopy were used to examine how hybridization affects the occupied-state onset and light absorption of the components. Frequency-dependent capacitance measurements were also to evaluated to determine whether a reliable flat-band potential could be assigned. The VB-XPS spectra give onset binding energies of 2.51, 2.63, and 2.56 eV for In-TCPP@$W_{18}O_{49}$, In-TCPP, and $W_{18}O_{49}$, respectively (Figures 3a–c). These values refer to the XPS binding-energy scale and are not electrochemical potentials versus NHE. The small differences between the spectra are consistent with changes in the electronic environment after hybridization, although they do not establish an absolute band alignment.

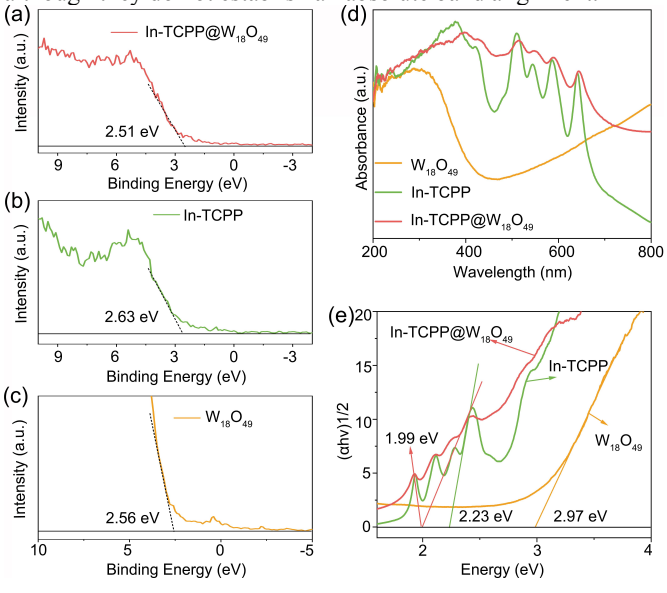


Figure 3. Valence-band XPS spectra of (a) In-TCPP@$W_{18}O_{49}$, (b) In-TCPP, and (c) $W_{18}O_{49}$. (d) UV–vis spectra and (e) corresponding Tauc plots of the three samples. The values in (a–c) indicate the fitted valence-band onset binding energies, and those in (e) indicate the apparent optical transition energies obtained by linear extrapolation.

The UV–vis spectrum of In-TCPP contains a strong Soret band in the near-UV region and several Q bands in the visible region, characteristic of the porphyrin π system (Figure 3d) [29, 47]. $W_{18}O_{49}$ shows broad visible-light absorption with a long-wavelength tail, commonly associated with oxygen-defect-related states [48–51]. In-TCPP@$W_{18}O_{49}$ retains the main spectral features of both components and absorbs across the near-UV and visible regions. The porphyrin bands remain visible at different In-TCPP loadings and solvothermal times (Figures S6 and S7), although their relative intensities vary with composition and preparation conditions. Analysis of the Tauc plots gives apparent optical transition energies of 2.23, 2.97, and 1.99 eV for In-TCPP, $W_{18}O_{49}$, and In-TCPP@$W_{18}O_{49}$, respectively (Figure 3e). These values are used only to compare the optical responses obtained with the adopted fitting procedure. Because the hybrid spectrum contains contributions from both components, the 1.99 eV value is not treated as a unique transport band gap and is not used to calculate an absolute conduction-band position.

To complement the optical measurements, the frontier orbitals of a molecular model representing In-TCPP were calculated (Figure S8). The HOMO and LUMO energies are −5.529 and −2.904 eV, respectively, giving a HOMO–LUMO gap of 2.625 eV. Both orbitals are mainly distributed over the porphyrin core. These results describe the molecular model rather than the band structure of the hybrid; the calculated orbital gap is not equated with the Tauc-derived transition energy.

Mott-Schottky measurements were recorded at 1000, 3000, and 5000 Hz (Figure S9). All three samples show positive-slope regions, but the curves are nonlinear over the full potential range and their extrapolated intercepts vary with frequency. We therefore do not assign a single flat-band potential to each sample or equate these intercepts with conduction-band positions. The evidence for interfacial charge redistribution and charge transfer is instead discussed on the basis of the XPS, photoelectrochemical measurements, and calculations in Section 3.2.

3.4. Selective Oxygen Reduction toward Photocatalytic H_2O_2 Production

The prepared catalysts were tested for photocatalytic H_2O_2 production under irradiation from a 300 W xenon lamp. The photocatalytic H_2O_2 production performance was first optimized by tuning the In-TCPP loading amount, and the measurements were conducted in pure water under ambient air, without adding any sacrificial agent. As shown in Figure 4a, all In-TCPP@$W_{18}O_{49}$ hybrids exhibit enhanced H_2O_2 generation compared with pristine $W_{18}O_{49}$ and In-TCPP, showing higher H_2O_2 production after hybridization of interfacial hybridization. Among the investigated samples, In-TCPP@$W_{18}O_{49}$-40 delivers the highest H_2O_2 production, reaching 2612 μmol g^{-1} after 150 min irradiation. This is further supported by electrochemical measurements, where In-TCPP@$W_{18}O_{49}$-40 exhibits a smaller charge-transfer resistance and a higher photocurrent response compared with the overloaded sample (Figure S10), indicating more efficient interfacial charge separation and transport. The corresponding H_2O_2 production rates summarized in Figure 4b further identify In-TCPP@$W_{18}O_{49}$-40 as the optimal catalyst composition. The H_2O_2 production data presented in Figure 4a-d were obtained using the Ce(IV) method. Independent measurements using the titanium sulfate colorimetric method gave similar production rates for In-TCPP@$W_{18}O_{49}$, In-TCPP, and $W_{18}O_{49}$ (Figure S11f). The calibration curve and corresponding spectra for the titanium sulfate method are provided in Figure S11a–e. The influence of solvothermal reaction duration on photocatalytic activity was further examined (Figure S8a, b). Among the investigated samples, In-TCPP@$W_{18}O_{49}$-5h exhibits the highest H2O2 production activity, indicating that an appropriate reaction duration affects the resulting photocatalytic activity for constructing an optimized interface. Consistently, EIS and transient photocurrent measurements (Figure S14a, b) reveal enhanced charge-transfer characteristics for the optimized 5h sample, further supporting the importance of appropriate interfacial construction. Additionally, the photocatalytic H_2O_2 generation of the optimized In-TCPP@$W_{18}O_{49}$-5h sample was evaluated in the presence of benzyl alcohol as a sacrificial agent. The catalyst achieved an H_2O_2 production rate of 35.2 mmol g-1 h-1 (Figure S12b), showing its activity under donor-assisted conditions photocatalytic capability under donor-assisted conditions.

The WO_3-based control shows lower photocatalytic activity, and its XRD pattern is consistent with crystalline WO_3 (Figure S15) [52, 53]. However, this comparison alone cannot establish the effect of oxygen vacancies because WO_3 and $W_{18}O_{49}$ differ in both phase and composition. We therefore compared In-TCPP@$W_{18}O_{49}$ hybrids prepared using supports treated under N_2 at 300 °C and in air at 300 and 400 °C (Figure S13). Under the same photocatalytic conditions, the H_2O_2 yield decreases in the order N_2–300 °C > Air–300 °C > Air–400 °C. This order matches the decrease in the relative double-integrated EPR intensity of the supports, supporting a contribution from vacancy-related defects to H_2O_2 production. A physical mixture of separately prepared In-TCPP and $W_{18}O_{49}$ gives a lower yield than the optimized hybrid, showing that simple mixing does not reproduce the activity achieved through hybrid synthesis. Time-dependent H_2O_2 accumulation and solar-to-chemical conversion (STC) efficiency were then measured for the optimized catalyst (Figure 4c). The H_2O_2 concentration increases continuously during irradiation, while the STC efficiency reaches 1.66% at the initial stage and approaches 1.31% after 2.5 h. The STC efficiencies were calculated from the experimentally measured H_2O_2 amounts and the measured incident optical power of 0.05 W, rather than from the nominal electrical power of the xenon lamp. The detailed calculation and all parameters are provided in the Supporting Information. Tafel measurements under electrochemical ORR conditions (Figure S11a) show faster reaction kinetics for In-TCPP@$W_{18}O_{49}$ compared with $W_{18}O_{49}$ and In-TCPP, consistent with improved interfacial charge transfer after coupling.

Just Accepted

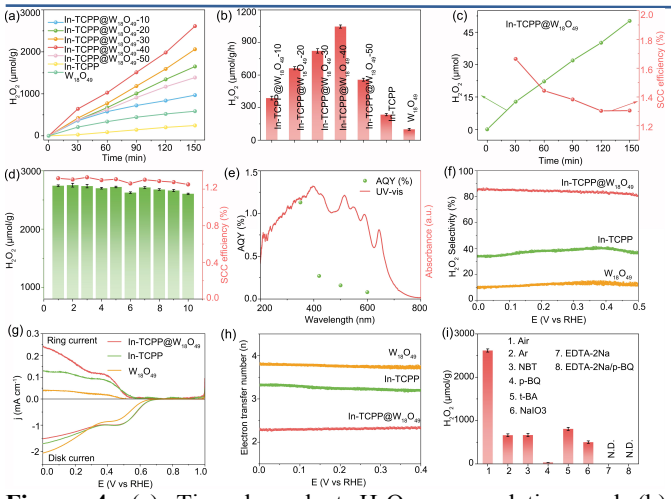


Figure 4. (a) Time-dependent H_2O_2 accumulation and (b) corresponding production rates of In-TCPP@$W_{18}O_{49}$ hybrids prepared with different $W_{18}O_{49}$ feed amounts, together with pristine In-TCPP and $W_{18}O_{49}$. (c) H_2 O_2 accumulation and solar-to-chemical conversion (STC) efficiency of the optimized hybrid. (d) H_2O_2 production and STC efficiency over ten consecutive cycles. (e) Wavelength-dependent apparent quantum yields (AQYs) measured in pure water without sacrificial reagents, together with the UV–vis absorption spectrum. (f) H_2O_2 selectivity, (g) disk and ring currents recorded during linear sweep voltammetry, and (h) electron-transfer numbers obtained from RRDE measurements. (i) H_2O_2 accumulation under different atmospheres and in the presence of scavengers. The suffixes -10, -20, -30, -40, and -50 denote the $W_{18}O_{49}$ feed amounts in milligrams. In-TCPP@$W_{18}O_{49}$-40 was prepared using 40 mg of $W_{18}O_{49}$ and a reaction time of 5 h and is identical to In-TCPP@$W_{18}O_{49}$-5h in the reaction-time comparison. The optimized sample is abbreviated as In-TCPP@$W_{18}O_{49}$ in panels (c–i). Error bars in panels (b), (d), and (i) represent the standard deviations of three independent photocatalytic experiments (n = 3).

Ten consecutive cycling tests show little change in the H_2O_2 production activity of In-TCPP@$W_{18}O_{49}$ (Figure 4d). The STC efficiency also remains similar during repeated operation. Additional cycling and long-term accumulation results are provided in Figures S17b and S17c. During the 40 h test, the cumulative H_2O_2 production reaches approximately 4078 μmol g^{-1}. The wavelength-dependent AQY was measured in pure water without sacrificial reagents (Figure 4e). The values were 1.13%, 0.27%, 0.16%, and 0.08% at 350, 420, 500, and 600 nm, respectively. For comparison, the AQY values measured in the presence of benzyl alcohol are provided separately in Figure S16. The H_2O_2 selectivity was further evaluated using RRDE measurements (Figure 4f). Compared with pristine In-TCPP and $W_{18}O_{49}$, In-TCPP@$W_{18}O_{49}$ maintains significantly higher H_2O_2 selectivity over the investigated potential range, reaching approximately 80%, suggesting that interfacial hybridization favors the selective two-electron oxygen reduction pathway.

RRDE measurements were performed under electrochemical polarization in an O_2-containing electrolyte with controlled mass transport, whereas photocatalysis used a suspended catalyst in pure water under ambient air without an external bias. Thus, the RRDE conditions do not directly reproduce the photocatalytic environment, where oxygen reduction is driven by photogenerated electrons and influenced by gas–liquid O_2 transfer. The approximately 80% H_2O_2 selectivity and electron-transfer number close to two are therefore regarded as supporting evidence for an intrinsic tendency toward the two-electron oxygen reduction pathway rather than a quantitative measure of photocatalytic selectivity. Electrochemical measurements were further performed to probe the oxygen reduction behavior. Figure 4g shows the disk and ring currents recorded for In-TCPP@$W_{18}O_{49}$ and its individual components. The calculated electron transfer number is approximately 2 over the tested potential range (Figure 4h), supporting a preferential two-electron oxygen reduction process. The photocatalytic H_2O_2 production performance of In-TCPP@$W_{18}O_{49}$ was further compared with representative WO_x and porphyrin-based photocatalysts reported previously (Table S1). Although the reported values vary with different reaction conditions, In-TCPP@$W_{18}O_{49}$ exhibits competitive performance under pure water and ambient air conditions without additional sacrificial agents, demonstrating the advantage of the designed oxygen-vacancy-mediated organic-inorganic interface.

Scavenger experiments were performed to examine how selected additives affect H_2O_2 accumulation (Figure 4i) [54–57]. Addition of nitro blue tetrazolium (NBT) or p-benzoquinone (p-BQ), which are commonly used to probe superoxide-related species, markedly decreased the measured H_2O_2 amount. Only a small amount of H_2O_2 was detected in the presence of p-BQ. For samples containing p-BQ, EDTA-2Na, or both, H_2O_2 was quantified using the KI-based spectrophotometric method and compared with Ce(IV) measurements (Figure S19 and Table S2). The two methods gave similar results for the p-BQ-containing sample and values close to zero for the EDTA-2Na and EDTA-2Na/p-BQ samples. Addition of tert-butanol (t-BA) caused a smaller decrease, whereas $NaIO_3$ also lowered H_2O_2 accumulation. The $NaIO_3$ result is consistent with competition for photogenerated electrons.

To examine the accompanying oxidation reaction, the reactor headspace was analyzed by GC-TCD under an Ar atmosphere (Figure S20). A signal assigned to O_2 appeared after irradiation of the In-TCPP@$W_{18}O_{49}$ suspension, while the response was much weaker in the dark, without photocatalyst, or after addition of EDTA-2Na. These observations are consistent with an accompanying water-oxidation process involving photogenerated holes.

RRDE measurements indicate a preference for two-electron oxygen reduction under the electrochemical test conditions (Figure 4f, h). Considered together with the scavenger results and the calculations discussed below, these data support a plausible stepwise two-electron route for photocatalytic H_2O_2 formation, consistent with recent reports of sequential single-electron-transfer steps within an overall two-electron ORR process [58]. In this pathway, adsorbed O_2 first undergoes a single-electron transfer to form $*O_2^-$, followed by protonation to *OOH and a second proton-coupled electron-transfer step that produces H_2O_2. The proposed stepwise two-electron reduction sequence is written as follows:

$$O_2 + e^- \rightarrow *O_2^- \quad (1)$$

$$*O_2^- + H^+ \rightarrow *OOH \quad (2)$$

$$*OOH + H^+ + e^- \rightarrow H_2O_2 \quad (3)$$

The accompanying oxidation half-reaction may be written as:

$$2H_2O + 4h^+ \rightarrow O_2 + 4H^+ \quad (4)$$

3.5. Role of Interfacial π–d Coupling in Oxygen Activation and H_2O_2 Formation

DFT calculations were performed to examine the effect of interfacial oxygen vacancies on the electronic interaction between In-TCPP and $W_{18}O_{49}$. Models with and without oxygen vacancies were compared. In the optimized structures (Figure 5a,

Just Accepted

b), the porphyrin N sites of In-TCPP are located near surface W atoms. Oxygen vacancy introduction induces local structural distortion and decreases the coordination number of adjacent W sites. The electronic origin of the interfacial interaction was further examined by spin-resolved PDOS and pCOHP analyses. Compared with the reference interface, the oxygen-vacancy-rich interface exhibits greater overlap between the C 2p states of In-TCPP and the W 5d states of $W_{18}O_{49}$ near the Fermi level (Figure 5c,d). This overlap indicates that the modified coordination environment around the vacancy-adjacent W sites strengthens their interaction with the porphyrinic π system. Consistent with the PDOS results, pCOHP analysis of a single interfacial W–C contact gives ICOHP values of −1.2 eV for the oxygen-vacancy-rich interface and −0.2 eV for the reference interface (Figure 5e,f). Because a more negative ICOHP value represents a stronger net bonding interaction, this difference indicates that the additional surface oxygen vacancies strengthen the selected W–C interaction. Together with the XPS shifts and charge-density redistribution, these results support oxygen-vacancy-enhanced coupling between the porphyrinic C 2p states and W 5d states at the interface. Similar effects of defect–molecule coupling and metal–conjugated-framework orbital hybridization on local electronic states and oxygen-intermediate adsorption have been reported in related photocatalytic systems [59, 60].

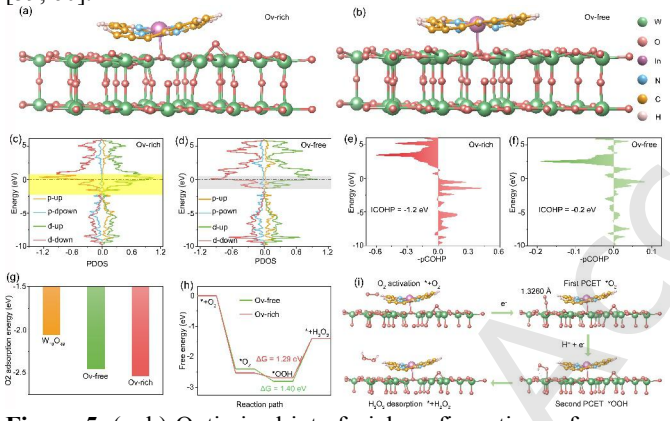


Figure 5. (a, b) Optimized interfacial configurations of oxygen-vacancy-rich (Ov-rich) and oxygen-vacancy-free (Ov-free) In-TCPP@$W_{18}O_{49}$ models. (c,d) Spin-resolved PDOS of the In-TCPP@$W_{18}O_{49}$ interfaces (c) with and (d) without additional surface oxygen vacancies, showing the contributions from the C 2p orbitals of In-TCPP and W 5d orbitals of $W_{18}O_{49}$. The Fermi level is set to 0 eV. (e,f) -pCOHP curves for a single interfacial W–C contact in the corresponding models. Positive and negative −pCOHP values denote bonding and antibonding contributions, respectively. The ICOHP values were integrated from -10 eV to the Fermi level. (g) Adsorption energies and adsorption configurations of $*O_2$ on $W_{18}O_{49}$, Ov-rich and Ov-free interfaces. (h) Gibbs free-energy profiles for O_2 adsorption and the two-electron oxygen reduction pathway on the reference and oxygen-vacancy-rich In-TCPP@$W_{18}O_{49}$ interfaces. The free energies were calculated using the computational hydrogen electrode model. (i) Schematic illustration of oxygen-vacancy-mediated π–d coupling associated with H_2O_2 formation through a stepwise two-electron oxygen reduction pathway.

To further evaluate the influence of interfacial electronic modulation on oxygen activation, the $*O_2$ adsorption behaviors of different models were compared (Figure 5g and Figure S21). The calculated $*O_2$ adsorption energies decrease from -2.06 eV for $W_{18}O_{49}$ to -2.46 and -2.54 eV for the Ov-free and Ov-rich interfaces, respectively, indicating that the introduction of In-TCPP strengthens O_2 adsorption, while oxygen vacancies further modulate the adsorption behavior. Consistently, the optimized adsorption configurations reveal a gradual elongation of the O–O bond from 1.3125 Å to 1.3172 Å and 1.3260 Å, suggesting progressively enhanced oxygen activation. Notably, $*O_2$ is not adsorbed directly at the oxygen-vacancy position but rather at an interfacial W site electronically influenced by nearby oxygen vacancies, indicating that oxygen vacancies promote oxygen activation primarily through electronic-structure modulation.

The thermodynamic effects of the additional surface oxygen vacancies on oxygen reduction were further examined using the computational hydrogen electrode model. As shown in Figure 5h, molecular O_2 adsorption is exergonic on both the reference and oxygen-vacancy-rich interfaces, with calculated adsorption free energies of approximately −2.4 to −2.6 eV. This result indicates thermodynamically favorable O_2 capture at the interface. After adsorption, formation of *OOH is also exergonic, whereas the subsequent proton–electron transfer that releases H_2O_2 is the largest uphill step of the $2e^-$ pathway. The competing $4e^-$ pathway was also considered by including O–O bond cleavage and the subsequent *O and *OH intermediates (Figure S22. For the $2e^-$ pathway, the largest uphill free-energy changes associated with *OOH conversion to H_2O_2 are 2.11 eV on the reference interface and 2.01 eV on the oxygen-vacancy-rich interface. The difference is modest but indicates slightly weakened *OOH stabilization after the introduction of additional surface oxygen vacancies. In the $4e^-$ pathway, O–O cleavage is thermodynamically downhill, but it leads to strongly stabilized *O and *OH intermediates. Consequently, conversion of *OH to H_2O becomes the largest uphill step, with free-energy changes of 2.38 and 2.25 eV on the reference and oxygen-vacancy-rich interfaces, respectively. These results suggest that, although O–O cleavage is thermodynamically accessible, completing sustained four-electron reduction is hindered by the strong stabilization of oxygenated surface intermediates. The calculated profiles are therefore used to describe thermodynamic trends rather than kinetic activation barriers. Surface activation of the H_2O_2 product is a separate, site-dependent process and may involve cleavage chemistry different from the ORR steps considered here [61]. Accordingly, H_2O_2 decomposition kinetics are not inferred from the present free-energy profiles. Based on these results, a stepwise two-electron ORR pathway was considered (Figure 5i). Adsorbed O_2 is first converted to *OOH through a proton-coupled electron-transfer step, followed by a second proton-coupled electron transfer that releases H_2O_2. The optimized *OOH adsorption configurations are shown in Figure S23. In both models, the O–O bond remains intact after *OOH formation, while the vacancy-containing interface slightly modifies the adsorption geometry and energetics of *OOH. Together with the PDOS and pCOHP results, the adsorption and free-energy analyses indicate that vacancy-enhanced π–d electronic coupling modulates the local electronic environment of the interfacial W site and thereby alters the adsorption and reaction thermodynamics of oxygen intermediates.

4 Conclusions

In summary, an oxygen-vacancy-rich In-TCPP@$W_{18}O_{49}$ hybrid was prepared for photocatalytic H_2O_2 production without sacrificial agents. The intimate organic–inorganic interface enhanced H_2O_2 formation and promoted the two-electron

In Accepted

oxygen reduction pathway. Experimental measurements and theoretical calculations show that oxygen vacancies modify the local electronic environment of adjacent W sites and strengthen the interaction between the porphyrin π states and W 5d orbitals. The resulting charge redistribution facilitates interfacial electron transfer and regulates the adsorption energies of $*O_2$ and *OOH intermediates. These changes promote selective H_2O_2 formation through the two-electron oxygen reduction process. These findings link oxygen vacancies and interfacial π–d coupling with oxygen-intermediate adsorption, providing a basis for designing organic–inorganic photocatalysts for selective H_2O_2 production.

Electronic Supplementary Material: Supplementary material (please provide the brief detail of the ESM) is available in the online version of this article at https://doi.org/10.26599/NR.2026.94909255.

Data availability

All data needed to support the conclusions in the paper are presented in the manuscript and/or the Electronic Supplementary Material. Additional data related to this paper may be requested from the corresponding author.

Acknowledgements

This work was financially supported by the Training Plan for Young Backbone Teachers in Colleges and Universities of Henan Province, China (No.2023GGJS139), the National Natural Science Foundation of China (No. 52671001; 12274011), Academic and Technical Leader Project of Henan University of Urban Construction (No. YCJXSJSDTR202307).

Declaration of competing interest

All the contributing authors report no conflict of interests in this work.

Author contribution statement

Yihong Zhang: Writing – original draft, Methodology, Data curation. Yilong Yang: Resources, Funding acquisition, Conceptualization. Haishan Zhu: Investigation, Formal analysis, Data curation. Yuen Zheng: Investigation, Formal analysis, Data curation. Jiaqi Shen: Investigation, Formal analysis, Data curation. Heju Guo: Investigation, Formal analysis, Data curation. Longzhou Jin: Investigation, Data curation. Liu Dan: Investigation, Data curation. Silin Liu: Investigation, Data curation. Junshu Wu: Resources, Data curation. Kaidong Xu: Resources, Data curation. Yong Zhao: Resources, Data curation. Songcan Wang: Writing – review & editing, Investigation. Chunqiang Zhuang: Writing – review & editing, Investigation, Conceptualization.

Use of AI statement

None

References

[1] Song, J.; Li, C.; Zhang, X.; Ma, P.; Zheng, K. Hydrogen peroxide production with photocatalysts based on carbon nitride: Evaluation criteria, reaction mechanism, improvement scheme, and development opportunity. *ACS Catal.*, 2025, **15**, 9058–9088.

[2] Yu, X.; Wei, Z.; Qin, Y.; Zhang, X.; Hao, D.; Jing, L.; Liu, Y.; Dai, H.; Deng, J.; Zhu, Y. Functional groups‐regulated organic semiconductors for efficient artificial photosynthesis of hydrogen peroxide. *Advanced Materials*, 2025, **37**, 2501494.

[3] Zhuang, C.; Zhang, A.; Zhang, Y.; Zhu, H.; Zhang, W.; Shan, P.; Xu, P.; Jin, Z.; Huang, H.; Li, S. Photocatalytic cocatalysts: Classification, structural design and crucial role in various reactions. *Coordination Chemistry Reviews*, 2025, **542**, 216867.

[4] Ren, P.; Liu, Y.; Nisar, I.; Das, S. Turning sunlight and seawater into energy: Photocatalytic hydrogen peroxide as a green fuel carrier. *Advanced Materials*, 2026, **38**, e72660.

[5] Zhuang, C.; Chang, Y.; Li, W.; Li, S.; Xu, P.; Zhang, H.; Zhang, Y.; Zhang, C.; Gao, J.; Chen, G.; Zhang, T.; Kang, Z.; Han, X. Light-induced variation of lithium coordination environment in g-C_3N_4 nanosheet for highly efficient oxygen reduction reactions. *ACS Nano*, 2024, **18**, 5206–5217.

[6] Shentu, Q.; Xing, K.; Li, K.; Han, N.; Li, Y. Recent Advances in H_2O_2 Electrosynthesis: From Catalyst Design and Interfacial Microenvironment Management to Reactor Engineering. *Advanced Functional Materials*, 2026, **36**, e18926.

[7] Jiang, Y.; Ni, P.; Chen, C.; Lu, Y.; Yang, P.; Kong, B.; Fisher, A.; Wang, X. Selective electrochemical H_2O_2 production through two‐electron oxygen electrochemistry. *Advanced Energy Materials*, 2018, **8**, 1801909.

[8] Zhao, Z.; Sun, R.; Wang, Y.; Jiang, Z.; Yan, D.; Zhang, R.; Liu, D.; Li, W.; Liu, Y. Fused‐ring acceptor–π–acceptor architecture enables near‐infrared‐absorbing mesoporous covalent organic frameworks for enhanced H_2O_2 photosynthesis. *Angewandte Chemie*, 2026, e5267333.

[9] Liu, X.; Zhan, X.; Ren, G.; Wu, Z.; Li, Z.; Qi, J.; Shi, G.; Xu, K.; Zeng, T.; Yu, M.; Cheng, S.; Gu, H.; Huang, H.; Zhu, M.; Xing, M.; Wang, H.; Zhu, W.; Zhang, W. Synergizing mass transfer and exciton dissociation in nanoscale COFs for efficient H_2O_2 photosynthesis. *Angew Chem Int Ed*, 2026, e6474422.

[10] Zhang, K.-L.; Chen, H.; Wang, L.; Tang, H.; Liu, Z.-Q. Tailoring the electron buffer in [zn−S−sm] units via gradient orbital hybridization for efficient H_2O_2 photosynthesis. *ACS Catal.*, 2026, 10773–10784.

[11] Chen, C.; Wang, Z.; Zhang, J.; Dai, K.; Zhang, J.; Zhang, L. Multi‐energy‐state covalent organic framework/sulfur‐vacancy‐engineered $Mn_{0.2}Cd_{0.8}$ S S‐scheme photocatalyst for enhanced light harvesting and H_2O_2 generation. *Advanced Materials*, 2026, e73326.

[12] Li, Z.; An, L.; Guan, L.; Yang, J.; Yin, R.; Jin, S.; Zhu, M.; Qin, J. Substituent-induced oxidation-reduction molecular organic junction for interfacial hydrogen peroxide photosynthesis. *Nat Commun*, 2026, **17**, 2794.

[13] Gao, Y.; Han, W.; Zhu, R.; He, Y.; Pang, H.; Zhang, J.; Gu, Z. Quaternary D‐π‐a covalent organic frameworks for high‐performance H_2O_2 photosynthesis. *Small*, 2026, **22**, e14074.

[14] Tian, T.; Wang, Y.; Wang, L.; Yuan, Z.; Yin, F.; Jiang, D.; Shen, Q.; Sun, Y.; Zhu, C.; Yuan, Y. Dual‐polarized donor–acceptor polymer unlocks long‐lived triplet excitons for high‐efficiency H_2O_2 photosynthesis. *Angewandte Chemie*, 2026, **138**, e21132.

[15] Kong, A.; Chen, Y.; Zou, Y.; Gu, J.; Liu, R.; Wei, G.; Yu, C. Coordination orientation isomerism boosting concerted hydrogen peroxide photosynthesis. *Nat Commun*, 2026, 6173.

[16] Yao, Y.; Liang, T.; Li, Z.; Wang, Z.; Wang, P.; Dou, T.; Chen, Z.; Li, Z.; Bian, J.; Jing, L. Carbon‐rich carbon nitride with synergistic gd‐N_4 sites and Z‐scheme heterojunction for non‐sacrificial hydrogen peroxide photosynthesis. *Adv Funct Materials*, 2026, **36**, e15298.

[17] Guo, H.; Wang, S.; Chen, X.; Kou, J.; He, G.; Dong, Z.; Yan, Y. Engineering a covalent organic framework-based type-II heterojunction for enhanced photocatalytic H_2O_2 synthesis. *Nat. Synth*, 2025, **4**, 1610–1620.

[18] Sun, N. A bifurcated dendritic $SrCO_3$-TiO_2/CdS heterostructure with oxygen vacancy for boosting photocatalytic $2e^-$ ORR of H_2O_2 production and simultaneous antibiotic degradation: Synergy and mechanism insight. 2025, **386**, 134185.

[19] Zheng, Y.; You, S.; Li, S.; Ding, Z.; Yuan, R.; Long, J.; Xu, C. All‐conjugated microporous polymer heterojunction with hierarchical hollow sphere architecture for photocatalytic H_2O_2 production. *Adv*

Just Accepted

Funct Materials, 2026, **36**, e08538.

[20] Li, C.; Song, J.; Guo, X.; Zhang, R.; Ma, P.; Zheng, K. Local charge enhancement at heterojunction interfaces caused by high‐density dislocations for improving photocatalytic H_2O_2 production. *Adv Funct Materials*, 2026, **36**, e25385.

[21] Zhang, H.; Wang, S.; Liu, H.; Zhang, Q.; Wu, X.; Wang, Y.; Xie, S. Asymmetric vacancies efficiently couple O_2 activation with reactive oxygen species evolution for enhanced photocatalytic methane conversion. *Angew Chem Int Ed*, 2026, e7358043.

[22] Meng, A.; Wu, X.; Lu, Z.; Gu, M.; Zhong, W.; Su, Y.; Yu, J. Accelerated interfacial charge transfer via ni 3D‐S 3p orbital hybridization in a CdS/NiPc S‐scheme heterojunction for highly‐selective H_2O_2 photosynthesis. 2026, e25871.

[23] Bian, Y.; Wang, Z.; Du, M.; Dai, K.; Yu, J.; Zhang, L. Strain‐amplified interfacial electric field in an S‐scheme Cu‐TCPP/CdSe heterojunction for efficient photocatalytic H_2O_2 production in pure water. *Adv Funct Materials*, 2026, **36**, e19493.

[24] Bao, C.-H.; Li, L.; Wang, X.-F.; Xia, S.-S.; Wang, X.; Jin, C.-C.; Chen, Z. Bringing porous framework materials toward photocatalytic H_2O_2 production. *Nano Lett.*, 2025, **25**, 4115–4136.

[25] Xue, Q.; Wang, Z.; Han, S.; Liu, Y.; Dou, X.; Li, Y.; Zhu, H.; Yuan, X. Ligand engineering of au nanoclusters with multifunctional metalloporphyrins for photocatalytic H_2O_2 production. *J. Mater. Chem. A*, 2022, **10**, 8371–8377.

[26] Dou, S.; Zhang, Y.; Xu, J.; Zhang, Y.; Lou, Y.; Zhang, J.; Dong, Y.; Zhu, Y.; Pan, C. Persistent semiquinone radicals enable efficient near-infrared-driven H_2O_2 photosynthesis. *Nat Commun*, 2026, **17**, 3333.

[27] Tong, Y.; Guo, H.; Liu, D.; Yan, X.; Su, P.; Liang, J.; Zhou, S.; Liu, J.; Lu, G. Q. (Max); Dou, S. X. Vacancy engineering of iron‐doped $W_{18}O_{49}$ nanoreactors for low‐barrier electrochemical nitrogen reduction. *Angewandte Chemie*, 2020, **132**, 7426–7431.

[28] Wang, S.; Wang, Y.; Song, Y.; Jia, X.; Yang, J.; Li, Y.; Liao, J.; Song, H. Immobilizing polysulfide via multiple active sites in $W_{18}O_{49}$ for Li-S batteries by oxygen vacancy engineering. *Energy Storage Materials*, 2021, **43**, 422–429.

[29] Cai, Z.; Liu, H.; Dai, J.; Li, B.; Yang, L.; Wang, J.; Zhu, H. Sunlight-driven simultaneous CO_2 reduction and water oxidation using indium-organic framework heterostructures. *Nat. Commun.*, 2025, **16**, 2601.

[30] Bao, T.; Tang, C.; Wu, Y.; Bi, Y.; Zhang, C.; Xi, Y.; Zou, Y.; Liu, C.; Yu, C. Photocatalytic co‐reduction of CO_2 and nitrate over porphyrin metal–organic frameworks: Dual atomic active site and nanostructure synergy enhances C–N coupling for urea production. *Angewandte Chemie*, 2025, **137**, e202512615.

[31] Li, Y.-X.; Hu, Y.; Bae, H.-S.; Du, J.; Zhao, S.; Pan, D.; Choi, W. Designing 1-nm-thick MOF nanosheets with donor–acceptor complexes for photosynthesis of H_2O_2 using water and dioxygen only. *ACS Nano*, 2024, **18**, 29233–29247.

[32] Shao, T.; Chang, Y.; Li, Z.; Song, Y.; Jin, D.; Gao, J.; Sun, L.; Hou, J. A chemically bonded and plasmonic Z-scheme junction for high-performance artificial photosynthesis of hydrogen peroxide. *J. Mater. Chem. A*, 2023, **11**, 1199–1207.

[33] Ren, L.; Yang, X.; Sun, X.; Yuan, Y. Synchronizing efficient purification of VOCs in durable solar water evaporation over a highly stable Cu/$W_{18}O_{49}$@graphene material. *Nano Lett.*, 2024, **24**, 715–723.

[34] Feng, C.; Tang, L.; Deng, Y.; Wang, J.; Liu, Y.; Ouyang, X.; Chen, Z.; Yang, H.; Yu, J.; Wang, J. Maintaining stable LSPR performance of $W_{18}O_{49}$ by protecting its oxygen vacancy: A novel strategy for achieving durable sunlight driven photocatalysis. *Applied Catalysis B: Environmental*, 2020, **276**, 119167.

[35] Su, H.; Yin, H.; Orbell, W.; Li, Y.; Wang, G.; Wang, Y.; Mori, K.; Chen, Z.; Li, H.; Yamashita, H.; Li, J. Asymmetric triple‐atom sites combined with oxygen vacancy for selective photocatalytic conversion of CO_2 to propionic acid. *Angewandte Chemie*, 2025, **137**, e202425446.

[36] Ji, X.; Wang, J.; Mei, L.; Tao, W.; Barrett, A.; Su, Z.; Wang, S.; Ma, G.; Shi, J.; Zhang, S. Porphyrin/SiO_2/Cp*rh(bpy)Cl hybrid nanoparticles mimicking chloroplast with enhanced electronic energy transfer for biocatalyzed artificial photosynthesis. *Adv Funct Materials*, 2018, **28**, 1705083.

[37] Zhang, Y.; Li, P.; Cui, P.; Hu, X.; Shu, C.; Sun, R.; Peng, M.; Tan, B.; Wang, X. Precisely constructing molecular junctions in hydrogen‐bonded organic frameworks for efficient artificial photosynthetic CO_2 reduction. *Angewandte Chemie*, 2024, **136**, e202413131.

[38] Wang, Y.; Guan, J.; Kumar, K.; He, W.; Valdez, J.; Yang, R.; Hu, G.; Huang, S.; Moores, A.; Meena, S. K.; Zhou, Y.; Liu, Y.; Ma, D. Room temperature photochemical synthesis of metal–organic frameworks for enhanced photocatalysis. *Nat Commun*, 2026, **17**, 4274.

[39] Zhu, Y.; Wu, F.; Zhang, X.; Lin, Y.; Zhang, L.; Chan, T.; Zhang, Q.; Chen, L. Engineering lattice distortion in ruthenium oxide enables robust acidic water oxidation via direct O–O coupling. *Advanced Materials*, 2025, **37**, 2500449.

[40] Zhang, Z.; Huang, J.; Fang, Y.; Zhang, M.; Liu, K.; Dong, B. A nonmetal plasmonic Z‐scheme photocatalyst with UV‐to NIR‐driven photocatalytic protons reduction. *Advanced Materials*, 2017, **29**, 1606688.

[41] Ruan, X.; Xu, M.; Zhang, X.; Ding, C.; Meng, D.; Leng, J.; Zhang, W.; Ravi, S. K.; Cui, X. Dual plasmonic fields enable high‐density hot‐electron generation with stepwise charge transfer directed to oxygen reduction sites for enhanced artificial photosynthesis of H_2O_2. *Advanced Energy Materials*, 2025, **15**, 2502302.

[42] Zhang, S.; Hu, R.; Xing, W.; Xue, S.; Xie, J.; Yan, R.; Wu, D.; Yang, C. Cascade reaction for Efficient $^1O_2$ generation enabled by spatially coupled vacancy pairs. *Angew Chem Int Ed*, 2026, e8870074.

[43] Xu, F.; He, Y.; Zhang, J.; Liang, G.; Liu, C.; Yu, J. Prolonging charge carrier lifetime via intraband defect levels in S‐scheme heterojunctions for artificial photosynthesis. *Angewandte Chemie*, 2025, **137**, e202414672.

[44] Gao, Y.; Zhan, Z.; Guo, L.; Li, Z.; Cai, S.; Wang, X.; Li, M.; Xie, Y.; Zhou, W. Visual location of oxygen vacancies on bismuth titanate nanosheets with periodic quantum well and promoting H_2O_2 photosynthesis. 2025.

[45] Zhang, H.; Wang, Y.; Zuo, S.; Zhou, W.; Zhang, J.; Lou, X. W. D. Isolated cobalt centers on $W_{18}O_{49}$ nanowires perform as a reaction switch for efficient CO_2 photoreduction. *J. Am. Chem. Soc.*, 2021, **143**, 2173–2177.

[46] Ma, J.; Miao, T. J.; Tang, J. Charge carrier dynamics and reaction intermediates in heterogeneous photocatalysis by time-resolved spectroscopies. *Chem. Soc. Rev.*, 2022, **51**, 5777–5794.

[47] Zeng, X.; Wang, T.; Wang, Z.; Tebyetekerwa, M.; Liu, Y.; Liu, Z.; Wang, G.; Wibowo, A. A.; Pierens, G.; Gu, Q.; Zhang, X. Fast photocatalytic hydrogen peroxide generation by singlet oxygen-engaged sequential excitation energy and electron-transfer process. *ACS Catal.*, 2024, **14**, 9955–9968.

[48] Choudhury, B.; Chetri, P.; Choudhury, A. Annealing temperature and oxygen-vacancy-dependent variation of lattice strain, band gap and luminescence properties of CeO_2 nanoparticles. *Journal of Experimental Nanoscience*, 2015, **10**, 103–114.

[49] Maarisetty, D.; Baral, S. S. Defect engineering in photocatalysis: Formation, chemistry, optoelectronics, and interface studies. *J. Mater. Chem. A*, 2020, **8**, 18560–18604.

[50] Cai, M.; Tong, X.; Liao, P.; Shen, S.; Zhao, H.; Li, X.; Xia, L.; Zhi, H.; Zhou, N.; Xue, Z.; Jin, L.; Li, J.; Li, G.; Dong, F.; Kabashin, A. V.; Wang, Z. M. Manipulating the optically active defect–defect interaction of colloidal quantum dots for carbon dioxide photoreduction. *ACS Catal.*, 2023, **13**, 15546–15557.

[51] Guo, H.-L.; Zhu, Q.; Wu, X.-L.; Jiang, Y.-F.; Xie, X.; Xu, A.-W. Oxygen deficient ZnO_{1-x} nanosheets with high visible light photocatalytic activity. *Nanoscale*, 2015, **7**, 7216–7223.

[52] Liu, J.; Crea, I.; Gobbato, T.; Rigodanza, F.; Rizzi, G. A.; Benazzi, E.; Bonchio, M. Organic‐inorganic photosynthetic interfaces built on intertwined WO_3 nanosheets for enhanced HBr/H_2O photoanodic oxidations. *Adv Energy and Sustain Res*, 2025, **6**, 2500184.

Just Accepted

[53] Liu, Y.; Cheng, M.; He, Z.; Gu, B.; Xiao, C.; Zhou, T.; Guo, Z.; Liu, J.; He, H.; Ye, B.; Pan, B.; Xie, Y. Pothole‐rich ultrathin WO_3 nanosheets that trigger N≡N bond activation of nitrogen for direct nitrate photosynthesis. *Angew Chem Int Ed*, 2019, **58**, 731–735.

[54] Ma, J.; Peng, C.; Peng, X.; Liang, S.; Zhou, Z.; Wu, K.; Chen, R.; Liu, S.; Shen, Y.; Ma, H.; Zhang, Y. H_2 O_2 photosynthesis from H_2O and O_2 under weak light by carbon nitrides with the piezoelectric effect. *J. Am. Chem. Soc.*, 2024, **146**, 21147–21159.

[55] Yang, S.; Si, D.; Zou, L.; Shi, M.; Huang, Y.; Cao, R. Engineering imine carbon catalytic sites in covalent organic frameworks for enhanced overall H_2O_2 photosynthesis. *J. Am. Chem. Soc.*, 2025, **147**, 30287–30295.

[56] Qin, F.; Zhang, C.; Qin, D.; Weng, H.; Duan, A.; Wang, H.; Huang, D.; Tang, L.; Zou, Y.; Zeng, G.; Wang, S. Condensation center regulation in donor–acceptor polymers enables dynamic proton reservoirs for efficient H_2 O_2 photosynthesis. *J. Am. Chem. Soc.*, 2026, **148**, 19684–19699.

[57] Liao, Q.; Sun, Q.; Xu, H.; Wang, Y.; Xu, Y.; Li, Z.; Hu, J.; Wang, D.; Li, H.; Xi, K. Regulating relative nitrogen locations of diazine functionalized covalent organic frameworks for overall H_2O_2 photosynthesis. *Angew Chem Int Ed*, 2023, **62**, e202310556.

[58] Peng, X.; Lei, B.; Tu, Z.; He, M.; Luo, Q.; Ding, T.; Wu, S.; Peng, G. Synergy of triphase interface engineering and electronic modulation of carbon nitride networks for continuous‐flow photosynthesis of H_2O_2. *Adv Funct Materials*, 2026, **36**, e22655.

[59] Dai, W.; Zhang, S.; Li, S.; Du, H.; Gao, J.; Xiao, S.; Xia, P.; Hu, S.; Li, H.; Liu, X.; Zheng, R.; Zhang, D. In situ generation and activation of H_2O_2 by metal-free catalysts for efficient gas phase NO removal. *Applied Catalysis B: Environment and Energy*, 2026, **399**, 127012.

[60] Hao, L.; Shen, R.; Huang, C.; Liang, G.; Zhang, P.; Li, X.; Liu, X. Nickel single atoms reconfigured 3D COFs boost H_2O_2 photosynthesis. *Angew Chem Int Ed*, 2026, **65**, e15814.

[61] Liu, X.; Li, S.; Ren, Z.; Cao, H.; Yang, Q.; Luo, Z.; He, L.; Zhao, J.; Wang, Q.; Li, G.; Liu, X.; Chen, L.; Li, H.; Zhang, D. Hydrogen peroxide heterolytic cleavage induced gas phase photo-fenton oxidation of nitric oxide. *Environ. Sci. Technol.*, 2024, **58**, 17797–17806.

© The Author(s) 2026. *Nano Research* published by Tsinghua University Press. The articles published in this open access journal are distributed under the terms of the Creative Commons Attribution 4.0 International License (http://creativecommons.org/licenses/by/4.0/), which permits use, distribution and reproduction in any medium, provided the original work is properly cited.

Just Accepted

Electronic Supplementary Material

Engineering molecular-semiconductor interfaces via vacancy-triggered π–d coupling for H_2O_2 photosynthesis

Yihong Zhang[1,2,5], Yilong Yang[1,6]✉, Haishan Zhu[2,3], Yuen Zheng[1], Jiaqi Shen[2,3], Heju Guo[1], Longzhou Jin[2,3], Dan Liu[2,3], Silin Liu[1], Junshu Wu[4], Kaidong Xu[1], Yong Zhao[5], Songcan Wang[6]✉, and Chunqiang Zhuang[2,3]✉

[1] *School of Materials and Chemical Engineering, Henan University of Urban Construction, Pingdingshan 467036, China*
[2] *Beijing Key Lab of Microstructure and Property of Advanced Materials, College of Material Science and Engineering, Beijing University of Technology, Beijing 100124, China*
[3] *Institute of Matter Science, Beijing University of Technology, Beijing 100124, China*
[4] *State Key Laboratory of Materials LoW–Carbon Recycling, College of Materials Science & Engineering, Beijing University of Technology, Beijing 100124, China*
[5] *Key Lab for Special Functional Materials of Ministry of Education, National & Local Joint Engineering Research Center for High-efficiency Display and Lighting Technology, School of Nano Science and Materials Engineering, Collaborative Innovation Center of Nano Functional Materials and Applications, Henan University, Kaifeng 475004, China*
[6] *State Key Laboratory of Flexible Electronics & School of Flexible Electronics, Northwestern Polytechnical University, 127 West Youyi Road, Xi'an 710072, China*

✉Address correspondence to Yilong Yang, ylyang@huuc.edu.cn; Songcan Wang, iamscwang@nwpu.edu.cn; Chunqiang Zhuang, chunqiang.zhuang@bjut.edu.cn

Supporting information to https://doi.org/10.26599/NR.2026.94909255

Just Accepted

1. Chemicals

Tungsten hexachloride (WCl_6, 99%), Indium nitrate hydrate ($In(NO_3)_3 \cdot xH_2O$), and 4,4′,4″,4‴-(Porphine-5,10,15,20-tetrayl) tetrakis(benzoic acid)(H_2TCPP, 99%) were purchased from Macklin Industrial Corporation. N,N-dimethylformamide (DMF, Analytical Reagent) was purchased from Zhengzhou Paini Chemical Reagent Factory. Ethanol (CH_3CH_2OH, 99%) was provided by Sinopharm Chemical Reagent Co., Ltd..

2. Material Characterization

The morphology and microstructure of the samples were observed by transmission electron microscopy (TEM, FEI Talos F200X). X-ray powder diffraction analysis was performed using an X-ray diffractometer (XRD, Bruker D8), and the functional groups of the samples were detected by Fourier-transform infrared spectroscopy (FTIR, Nicolet iS50, Thermo Fisher Scientific). Steady-state photoluminescence (PL) spectra were collected on a fluorescence spectrometer (F-7000, Hitachi, Japan), while time-resolved PL spectra were recorded on an Edinburgh steady-state/transient fluorescence spectrometer (FLS 980). UV–vis absorption spectra were acquired using a Shimadzu UV-2600 spectrophotometer. Electron spin resonance (ESR) analysis was conducted on a Bruker A300-10/12 ESR spectrometer. The surface chemical states of the samples were analyzed by X-ray photoelectron spectroscopy (XPS) using a Thermo Fisher Scientific ESCALAB Xi+ spectrometer.

3. Synthesis of reaction-time-dependent In-TCPP@W18O49 samples

Following a similar procedure, $In(NO_3)_3 \cdot xH_2O$ (30 mg, 0.10 mmol) and H_2TCPP (32.0 mg, 0.04 mmol) were dispersed in DMF (10.0 mL), followed by the addition of 40 mg of pre-synthesized $W_{18}O_{49}$. The resulting mixture was ultrasonicated for 10 min to remove air bubbles and then heated to 130 °C in an oil bath for different reaction times: 3.0, 4.0, 5.0, and 6.0 h. After workup using the same procedure, the products were denoted as In-TCPP@$W_{18}O_{49}$-3h, In-TCPP@W18O49-4h, In-TCPP@W18O49-5h, and In-TCPP@$W_{18}O_{49}$-6h, respectively. The suffixes -3h, -4h, -5h, and -6h indicate the solvothermal reaction times, while the $W_{18}O_{49}$ feed amount was fixed at 40 mg for all samples in this series. Consequently, In-TCPP@$W_{18}O_{49}$-5h and In-TCPP@$W_{18}O_{49}$-40 correspond to the same preparation condition, namely 40 mg of $W_{18}O_{49}$ and a reaction time of 5 h. This sample gave the highest H_2O_2 production in both optimization series and is referred to as In-TCPP@$W_{18}O_{49}$ without a suffix elsewhere in the manuscript unless otherwise specified.

4. Synthesis of In-TCPP@$W_{18}O_{49}$ using air-treated supports

Pre-synthesized $W_{18}O_{49}$ was heated in air at 300 or 400 °C for 2h and then cooled to room temperature. The resulting supports were designated as Air-300 °C and Air-400 °C, respectively. For hybrid synthesis, $In(NO_3)_3 \cdot xH_2O$ (30 mg, 0.10 mmol) and H_2TCPP (32.0 mg, 0.04 mmol) were dispersed in DMF (10.0 mL), followed by the addition of 40 mg of the corresponding air-treated support. The mixture was ultrasonicated for 10 min and heated in an oil bath at 130 °C for 5.0 h. The products were collected, washed, and dried using the same procedure as for the optimized In-TCPP@ $W_{18}O_{49}$ hybrid. In the comparative measurements, N_2 -300 °C, Air-300 °C, and Air-400 °C identify the treatment conditions of the $W_{18}O_{49}$ supports used to prepare the hybrids.

5. Preparation of the In-TCPP/ $W_{18}O_{49}$ physical mixture

Separately prepared In-TCPP (7.80 mg) and $W_{18}O_{49}$ (40.0 mg) were mixed. This ratio was selected to match the In-TCPP fraction estimated from the ICP-OES W content of the optimized hybrid, assuming a binary composition of In-TCPP and $W_{18}O_{49}$. Ethanol was added, and the powders were ground together for 30 min. The mixture was then dried at 60 ℃ for 12 h under vacuum and labeled “Physical mixture”.

6. Synthesis of In-TCPP@WO_3 control sample

For comparison, an In-TCPP@WO_3 control sample was synthesized using the same procedure as that for In-TCPP@$W_{18}O_{49}$. $In(NO_3)_3 \cdot xH_2O$ (30 mg, 0.10 mmol) and H_2TCPP (32.0 mg, 0.04 mmol) were dispersed in DMF (10.0 mL), followed by the addition of 40 mg of pre-synthesized WO_3. The resulting mixture was ultrasonicated for 10 min to remove air bubbles and then heated to 130 °C in an oil bath for 5.0 h. After the reaction, the product was collected and washed using the same workup procedure, and the obtained sample was denoted as In-TCPP@WO_3.

7. Photocatalytic H_2O_2 Production

5 mg of the catalyst sample was ultrasonically dispersed in 40 mL of deionized water to form a homogeneous suspension. A 300 W xenon lamp (Perfectlight, PLS-SX300E, Beijing, China) was employed as the light source to trigger the photocatalytic reaction. The suspension was then transferred into a reactor and continuously stirred under ambient air while being exposed to light irradiation for the photocatalytic reaction. At 30 min intervals, 1 mL aliquots of the reaction solution were collected, centrifuged, and subsequently used for quantitative analysis. The concentration of H_2O_2 was determined by redox titration using ferrous phenanthroline as an indicator and cerium(IV) sulfate as the titrant, based on the following reaction:

$$2Ce^{4+} + H_2O_2 \rightarrow 2Ce^{3+} + 2H^+ + O_2 \quad (1)$$

8. Determination of H_2O_2 by KI-based spectrophotometry

The KI-based spectrophotometric method was used to determine H_2O_2 in photocatalytic samples containing p-BQ, EDTA-2Na, or both. After removal of the catalyst, a 3 mL aliquot of the supernatant was mixed with 1.0 mL of 0.10 mol L^{-1} potassium hydrogen phthalate solution and 1.0 mL of 0.40 mol L^{-1} KI solution. The mixture was allowed to stand for 30 min before UV–vis measurement. Under acidic conditions, H_2O_2 oxidizes iodide to triiodide:

$$H_2O_2 + 3I^- + 2H^+ \rightarrow I_3^- + 2H_2O \quad (2)$$

The absorbance at 350 nm was used to determine the H_2O_2 concentration from a calibration curve obtained with H_2O_2 standards

Just Accepted

subjected to the same reagent additions and reaction time. Dilution during sample preparation was included in the calculation. The results were compared with those obtained using the Ce(IV) method.

9. Determination of H_2O_2 by titanium sulfate colorimetry

Titanium sulfate colorimetry was used to cross-check the H_2O_2 yields measured by the Ce(IV) method for samples without scavengers. The color reagent was prepared by dissolving 4.5 g of $Ti(SO_4)_2$ in 250 mL of 0.40 mol L^{-1} H_2SO_4. After removal of the catalyst, 2.0 mL of the reaction solution was combined with 2.0 mL of the color reagent and left for 5 min. The yellow peroxide complex formed with Ti(IV) was measured by UV–vis spectroscopy at 410 nm. H_2O_2 concentrations were calculated using a calibration curve prepared by treating H_2O_2 standards in the same manner, with correction for dilution.

10. Solar-to-chemical Energy Conversion (STC) Efficiency Measurement

A 20 mg portion of the photocatalyst was dispersed in 60 mL of deionized water. A 300 W xenon lamp equipped with a PLS-LA320A diffuser was used as the light source. The irradiance measured at the reactor position was 50 mW cm^{-2}, and the illuminated area was approximately 1.0 cm^2 (1.0×10^{-4} m^2). The incident optical power was therefore:

$$P_{\text{in}} = I \times A = 50 mW cm^{-2} = 0.050 W \tag{3}$$

The nominal electrical power of the xenon lamp was not used in the STC calculation. At each irradiation time, the amount of H_2O_2 was determined experimentally from its measured concentration:

$$\text{n}_{H_2O_2} = C_{H_2O_2} \times V \tag{4}$$

where V=0.060 L. The STC efficiency was calculated using:

$$\eta_{STC}(\%) = \frac{\Delta G^0_{H_2O_2} \times n_{H_2O_2}}{P_{in} \times t} \times 100\% \tag{5}$$

where $\Delta G^0_{H_2O_2}$ = 117 kJ mol^{-1} is the standard Gibbs free-energy change adopted for H_2O_2 formation, $n_{H_2O_2}$ is the experimentally measured amount of H_2O_2, P_{in} = 0.050 W is the incident optical power, and t is the irradiation time in seconds. The reported maximum efficiency of 1.66% and the stabilized value of approximately 1.31% were calculated from the experimentally measured H_2O_2 production data, rather than from a theoretical production rate.

11. Apparent Quantum Yield Measurements

5 mg of the catalyst sample was ultrasonically dispersed in a mixture of 35 mL of deionized water and 5 mL of benzyl alcohol to form a homogeneous suspension. A 300 W xenon lamp was used as the light source to irradiate the reactor for 1 hour under magnetic stirring, with the incident light passing through band-pass filters centered at 350 ± 15 nm, 420 ± 15 nm, 500 ± 15 nm, and 600 ±15 nm, respectively. The light intensity was measured using a light power meter with an irradiated area of 4π cm^2. The apparent quantum yield (AQY) was calculated according to the following equation:

$$AQY = \frac{H_2O_2\ formed\ (mol) \times 2}{N} \tag{7}$$

12. Electrochemical Measurements

Transient photocurrent and electrochemical impedance spectroscopy (EIS) measurements were performed using a three-electrode system (CHI660E, Shanghai, China). A graphite rod served as the counter electrode, a saturated calomel electrode (SCE) as the reference electrode, and 0.1 M Na2SO4 aqueous solution as the electrolyte. The working electrode was prepared as follows: 5 mg of the catalyst, 2 mL of ethanol, and 90 μL of Nafion solution were mixed and ultrasonicated to form a homogeneous slurry. Then, 40 μL of the slurry was drop-cast onto a fluorine-doped tin oxide (FTO) glass slide and dried overnight in a vacuum oven.

Rotating ring-disk electrode (RRDE) measurements were carried out using a PINE RRDE assembly connected to a BioLogic electrochemical workstation. A saturated calomel electrode (SCE) and a Pt mesh were used as the reference and counter electrodes, respectively. The catalyst ink was prepared by dispersing 5.0 mg of catalyst in a mixture of 1.0 mL of ethanol and 50 μL of Nafion solution, followed by ultrasonication for 60 min. A 12 μL aliquot of the resulting ink was deposited onto the glassy carbon disk and dried at room temperature.

The measurements were performed at room temperature in O_2-saturated 0.1 M KOH (pH ≈ 13.0). Potentials measured against SCE were converted to the reversible hydrogen electrode scale according to:

$$E_{RHE} = E_{SCE} + 0.059\text{p}H + 0.242 \tag{8}$$

Linear sweep voltammograms were recorded at a scan rate of 10 mV s^{-1} and a rotation rate of 1600 rpm. The Pt ring potential was held at 1.2 V versus RHE to detect H_2O_2 generated at the disk electrode. Background currents were recorded in N_2-saturated 0.1 M KOH under the same scan rate, rotation rate, and ring-potential conditions. The corresponding background currents were subtracted from the disk and ring currents measured in O_2-saturated electrolyte.

The manufacturer-specified geometric collection efficiency of the PINE RRDE, N=0.37 was used. The H_2O_2 selectivity and electron-transfer number were calculated as follows:

$$H_2O_2\ selectivity(\%) = \frac{2\frac{I_r}{N}}{I_d + \frac{I_r}{N}} \times 100\% \tag{9}$$

Just Accepted

$$n = \frac{4I_d}{I_d + \frac{I_r}{N}} \quad (10)$$

where I_d, I_r, and N represent the background-corrected disk current, ring current, and ring collection efficiency, respectively.

13. Computational Methods

All density functional theory (DFT) calculations were performed using the Vienna Ab initio Simulation Package (VASP, version 6.4.2) with the projector augmented-wave (PAW) method. The exchange–correlation energy was treated within the generalized gradient approximation (GGA) using the Perdew–Burke–Ernzerhof (PBE) functional. Valence electrons were expanded in a plane-wave basis with a kinetic energy cutoff of 450 eV. The PAW potentials were W_sv, O, C, H, N and In_d, treating 14, 6, 4, 1, 5 and 13 valence electrons, respectively. Dispersion interactions were included using Grimme's DFT-D3 method with zero damping. Spin-polarized calculations were performed throughout. Partial occupancies of the Kohn–Sham orbitals were treated with Gaussian smearing and a smearing width of 0.02 eV. The Brillouin zone of the slab supercell was sampled at the Γ point (a 1 × 1 × 1 Monkhorst–Pack mesh). Electronic self-consistency was converged to 10^{-5} eV, and ionic relaxations were performed using the conjugate-gradient algorithm until the residual forces on all unconstrained atoms were smaller than 0.03 eV $Å^{-1}$. The cell shape and volume were kept fixed during relaxation.

The In-TCPP@$W_{18}O_{49}$ interface was modeled as a periodic slab heterostructure. A three-layer $W_{18}O_{49}$ slab containing 54 W atoms (18 W atoms per layer) was used, with an in-plane supercell of a = 14.03 Å, b = 17.70 Å and γ = 69.4° and a vacuum spacing of approximately 15 Å was introduced along the z direction to avoid spurious interactions between periodic images. To reduce the computational cost while retaining the catalytically relevant coordination environment, the In-TCPP unit was represented by an indium porphyrin core (In–N_4, $C_{20}H_{12}N_4In$) adsorbed on the $W_{18}O_{49}$ surface. In this interface model, the porphyrin plane lies approximately parallel to the slab, the In center is coordinated to four pyrrolic nitrogen atoms (In–N ≈ 2.09–2.22 Å), and In is additionally anchored to a surface lattice oxygen atom of $W_{18}O_{49}$ (In–O ≈ 2.31 Å). During geometry optimization, the bottom two $W_{18}O_{49}$ layers were frozen , whereas the topmost $W_{18}O_{49}$ layer, the In–N_4 unit and all adsorbates were fully relaxed. Reaction intermediates, including O*, OH*, *O+*O, *OOH, *O_2 and *H_2O_2, were adsorbed on the $W_{18}O_{49}$ surface of the heterostructure.

Oxygen-deficient models were constructed from the same interface supercell by removing two surface lattice oxygen atoms from the topmost atomic layer of $W_{18}O_{49}$. The vacancies are located in the vicinity of the In–N_4 center (approximately 3.7 and 4.1 Å from In), while the interfacial oxygen atom that directly anchors In to the surface was retained. After vacancy creation, the top $W_{18}O_{49}$ layer, the In–N_4 unit and the adsorbates were re-optimized with the same computational settings as for the pristine interface. No artificial charge was added to the supercell, and the vacancy-containing slabs were treated as charge-neutral systems.

The Gibbs free-energy change (Δ*G*) of each elementary step was evaluated as

$$\Delta G = \Delta E + \Delta E_{ZPE} - T\Delta S + \Delta G_U + \Delta G_{PH} \quad (11)$$

where Δ*E* is the DFT total-energy difference, ΔE_{ZPE} is the zero-point-energy correction obtained from harmonic vibrational frequencies of the adsorbed intermediates, *T* is the temperature (298.15 K), and Δ*S* is the entropy change. For adsorbed species, only vibrational contributions to the entropy were considered within the harmonic approximation. For gas-phase molecules (H_2, H_2O and H_2O_2), the enthalpic and entropic corrections were taken from standard thermodynamic tables.

Just Accepted

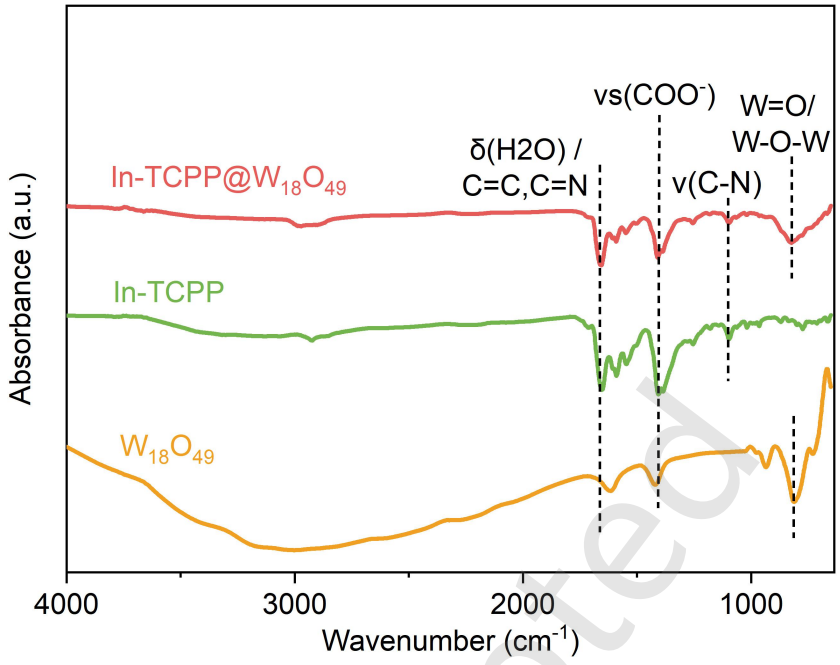


Figure S1. FT-IR spectra of $W_{18}O_{49}$, In-TCPP, and In-TCPP@$W_{18}O_{49}$.

Just Accepted

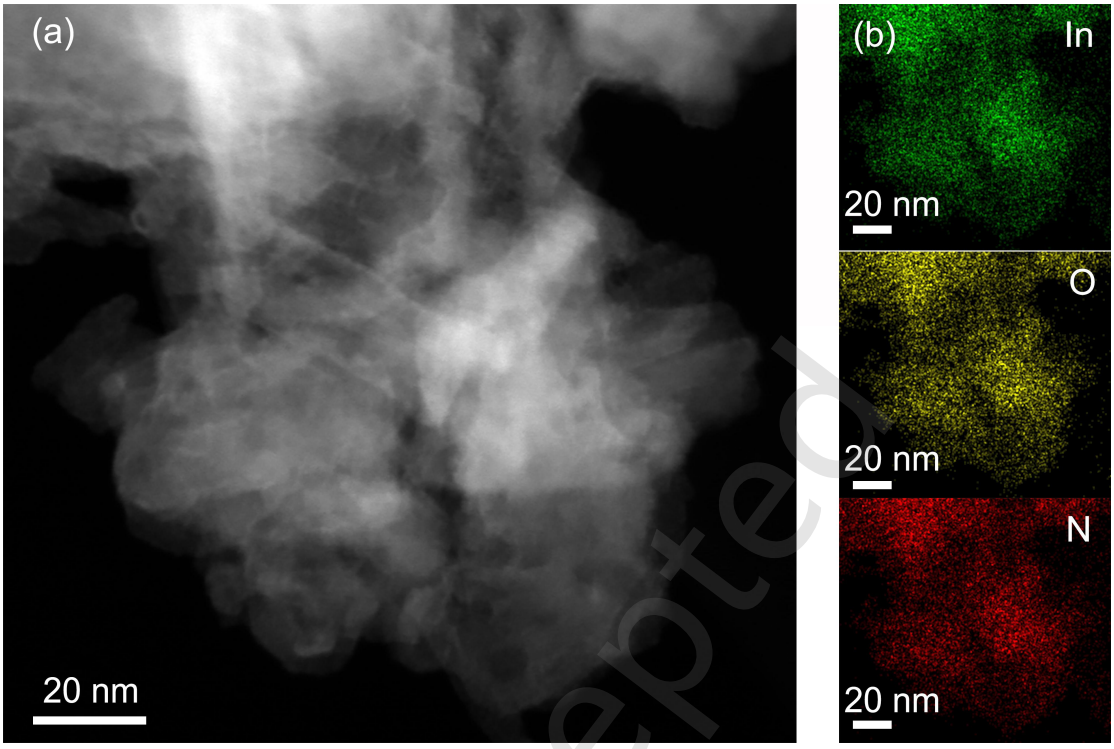


Figure S2. (a) HAADF image of In-TCPP. (b) STEM-EDS elemental mapping of In-TCPP.

Just Accepted

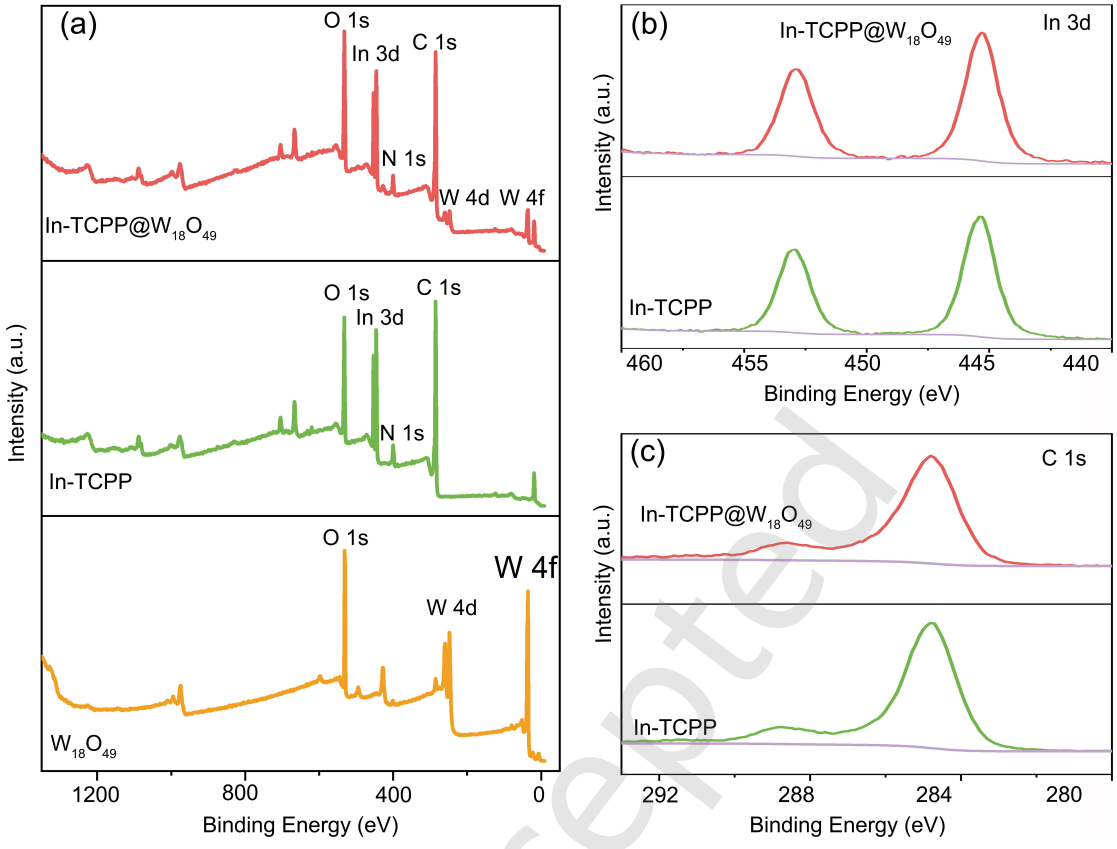


Figure S3. (a) XPS survey spectra of the samples. High-resolution XPS spectra of (b) In 3d and (c) C 1s for pristine In-TCPP and In-TCPP@$W_{18}O_{49}$.

Just Accepted

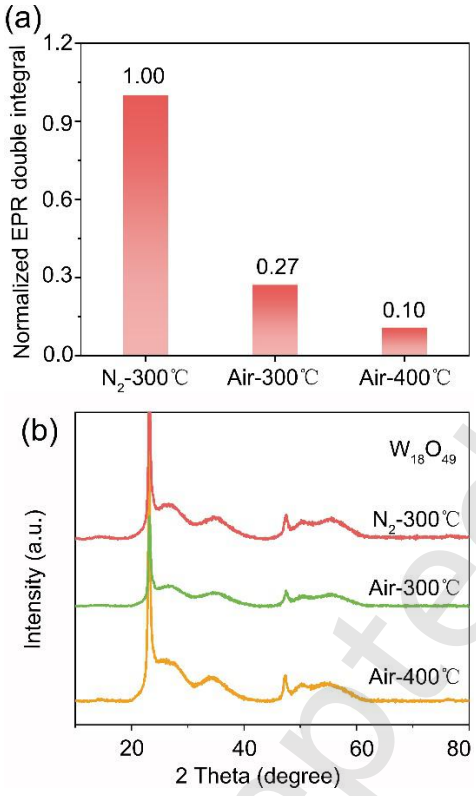


Figure S4. (a) Relative double-integrated EPR intensities of $W_{18}O_{49}$ samples treated under N_2 at 300 °C and in air at 300 and 400 °C, normalized to the N_2–300 °C sample. (b) XRD patterns of $W_{18}O_{49}$ samples treated under N_2 at 300 °C and in air at 300 °C and 400 °C.

Just Accepted

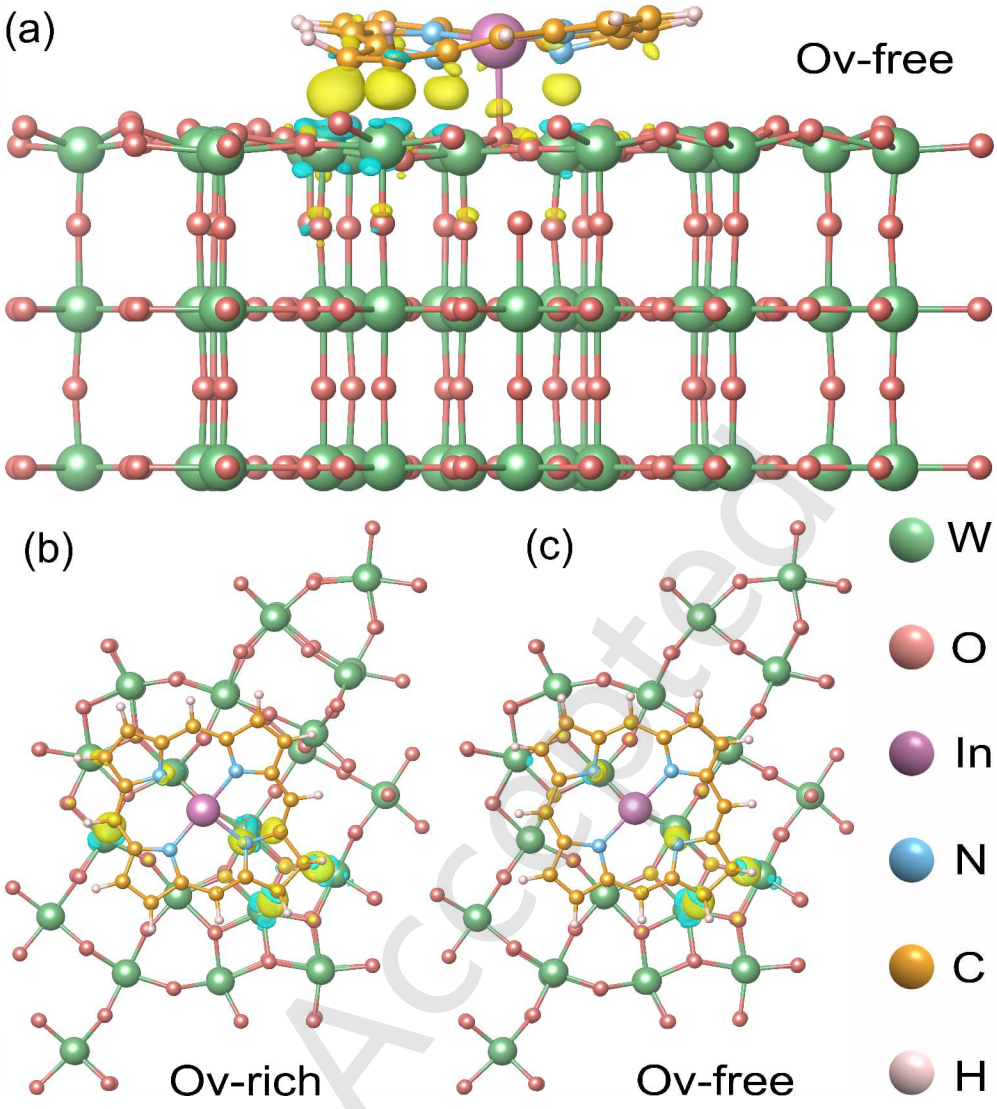


Figure S5. Differential charge density distributions of In-TCPP@$W_{18}O_{49}$ interfaces with and without oxygen vacancies. (a) Side view of the oxygen-vacancy-free model. Top views of (b) oxygen-vacancy-rich and (c) oxygen-vacancy-free interfaces. Yellow and cyan regions represent electron accumulation and depletion, respectively. An isovalue of 0.01 e $Å^{-3}$ was used for all panels.

Just Accepted

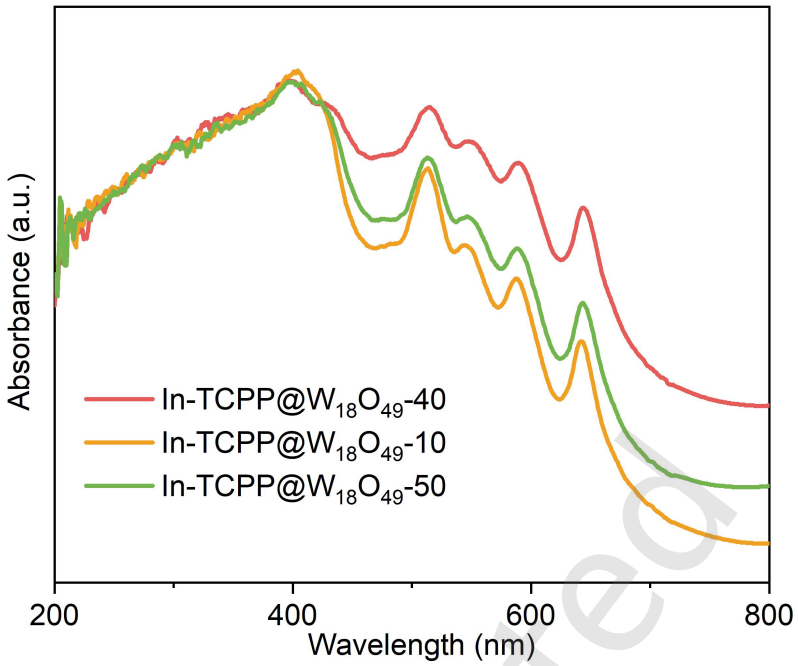


Figure S6. UV–vis absorption spectra of In-TCPP@$W_{18}O_{49}$ composites synthesized with different In-TCPP and $W_{18}O_{49}$ ratios.

Just Accepted

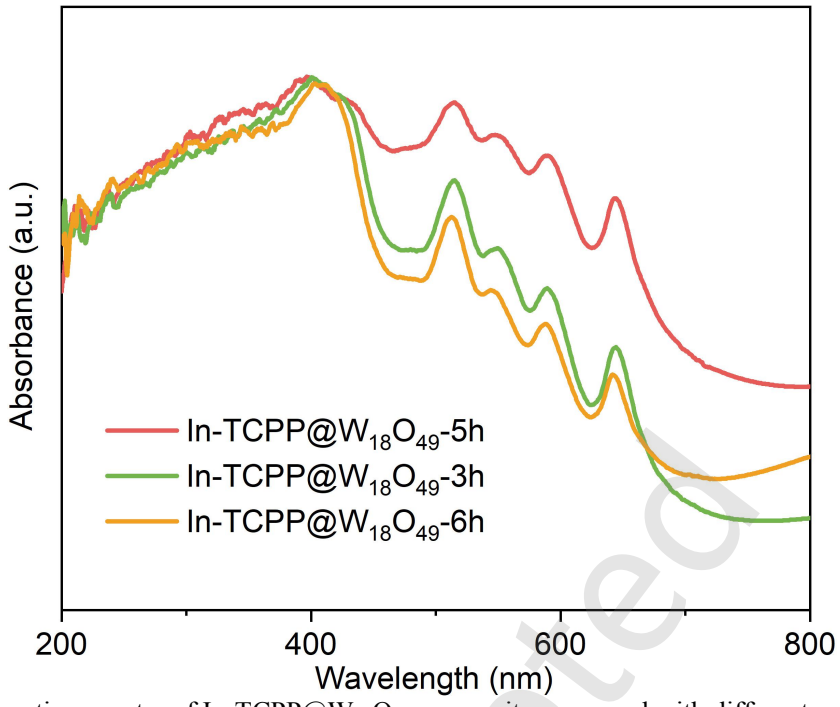


Figure S7. UV–vis absorption spectra of In-TCPP@$W_{18}O_{49}$ composites prepared with different solvothermal reaction durations.

Just Accepted

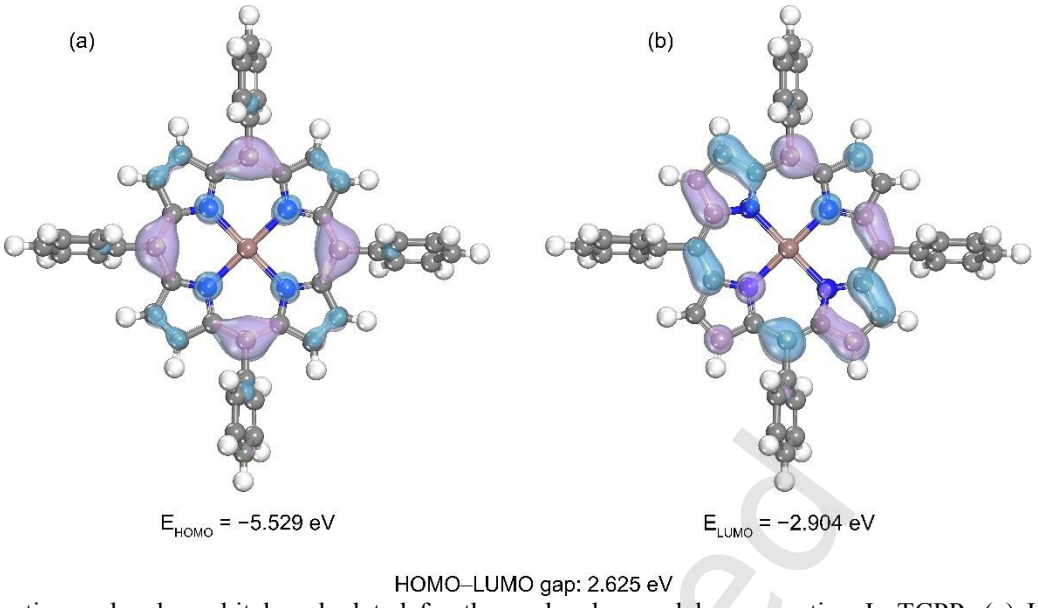


Figure S8. Frontier molecular orbitals calculated for the molecular model representing In-TCPP: (a) HOMO and (b) LUMO. The corresponding orbital energies are −5.529 and −2.904 eV, with a HOMO–LUMO gap of 2.625 eV. Cyan and purple indicate opposite phases of the orbital wavefunctions.

Just Accepted

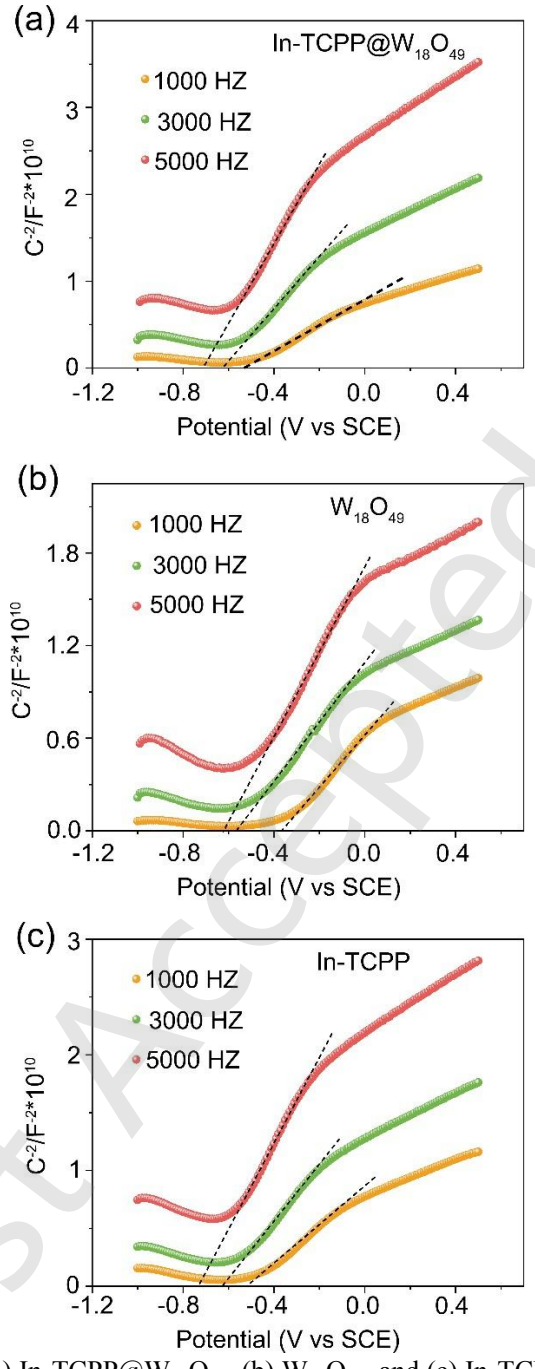


Figure S9. Mott–Schottky plots of (a) In-TCPP@$W_{18}O_{49}$, (b) $W_{18}O_{49}$, and (c) In-TCPP measured at 1000, 3000, and 5000 Hz. Dashed lines show linear fits to selected positive-slope regions and their extrapolation to the potential axis. Potentials are referenced to SCE. The frequency-dependent intercepts are not assigned as unique flat-band potentials.

Just Accepted

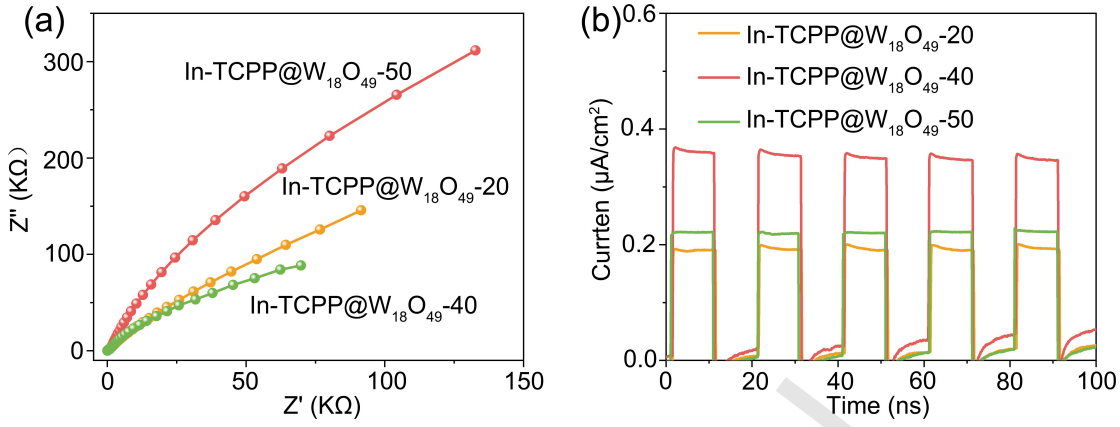


Figure S10. (a) Electrochemical impedance spectroscopy (EIS) Nyquist plots of In-TCPP@$W_{18}O_{49}$-20, -40, and -50 samples. (b) Transient photocurrent responses (I-t curves) of the corresponding samples under intermittent light irradiation.

Just Accepted

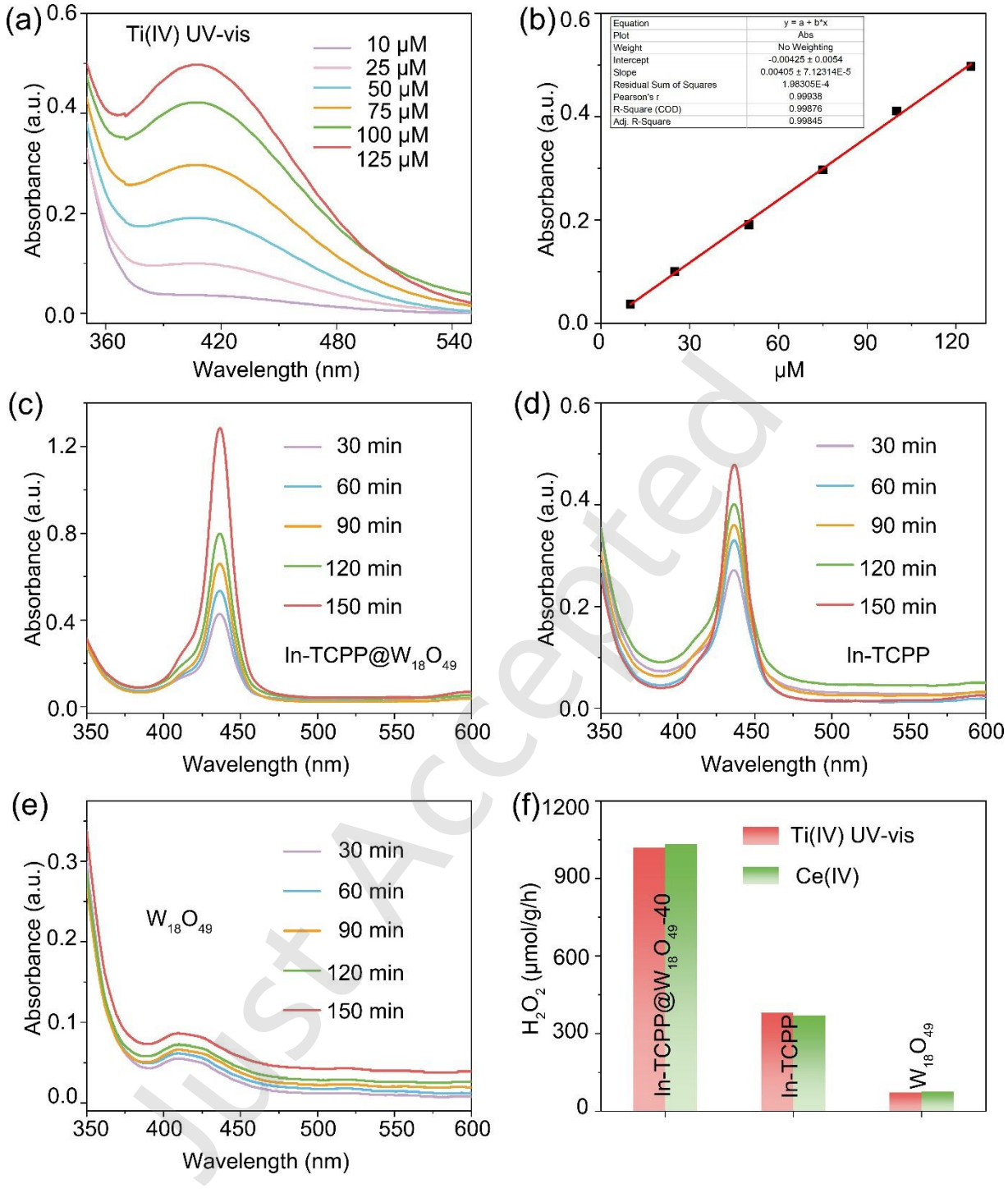


Figure S11. (a) UV–vis spectra of H_2O_2 standards after reaction with titanium sulfate and (b) the corresponding calibration curve. (c–e) Spectra obtained using the titanium sulfate method for reaction samples collected at different irradiation times from (c) In-TCPP@$W_{18}O_{49}$, (d) In-TCPP, and (e) $W_{18}O_{49}$. (f) H_2O_2 production rates determined by the titanium sulfate and Ce(IV) methods. Photocatalytic experiments were conducted in pure water under ambient air without sacrificial reagents. The hybrid shown here is the optimized sample prepared using 40 mg of $W_{18}O_{49}$ and a solvothermal reaction time of 5 h.

Just Accepted

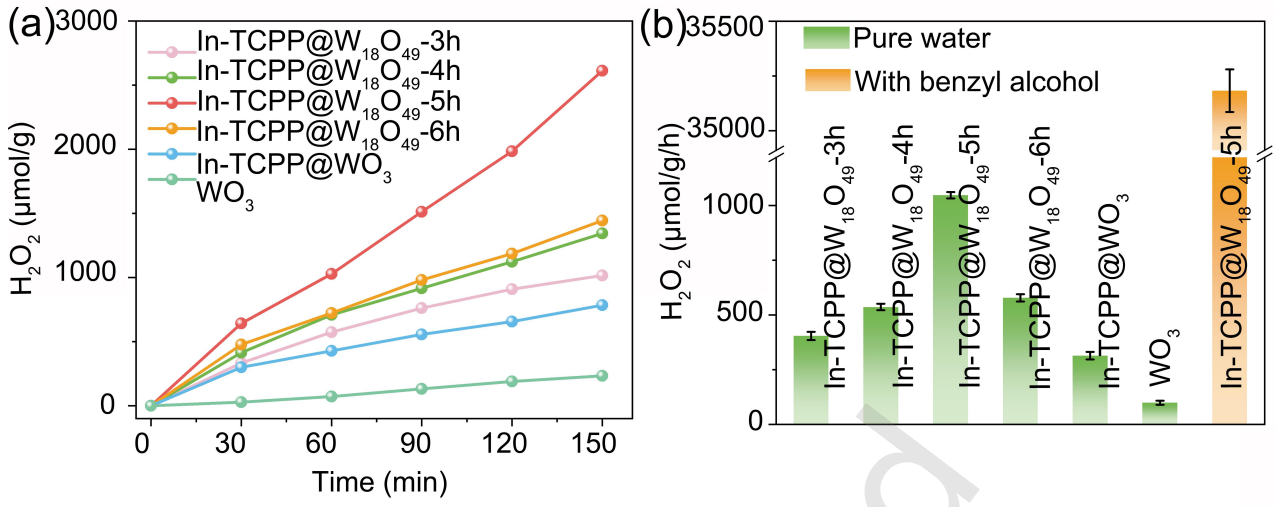


Figure S12. (a) H_2O_2 accumulation in pure water for In-TCPP@$W_{18}O_{49}$ prepared at different solvothermal reaction times, together with In-TCPP@WO_3 and WO_3 controls. (b) Corresponding production rates in pure water and the production rate of the optimized hybrid in the presence of benzyl alcohol. The suffixes -3h, -4h, -5h, and -6h denote solvothermal reaction times of 3, 4, 5, and 6 h, respectively. The reaction-time series was prepared using 40 mg of $W_{18}O_{49}$. Thus, In-TCPP@$W_{18}O_{49}$-5h corresponds to In-TCPP@$W_{18}O_{49}$-40 in the feed-amount series. H_2O_2 was quantified using the Ce(IV) method. The rate was measured under pure water conditions (green bars) and in the presence of benzyl alcohol as a sacrificial agent (yellow bar). Error bars in panel (b) represent the standard deviations of three independent photocatalytic experiments (n = 3).

Just Accepted

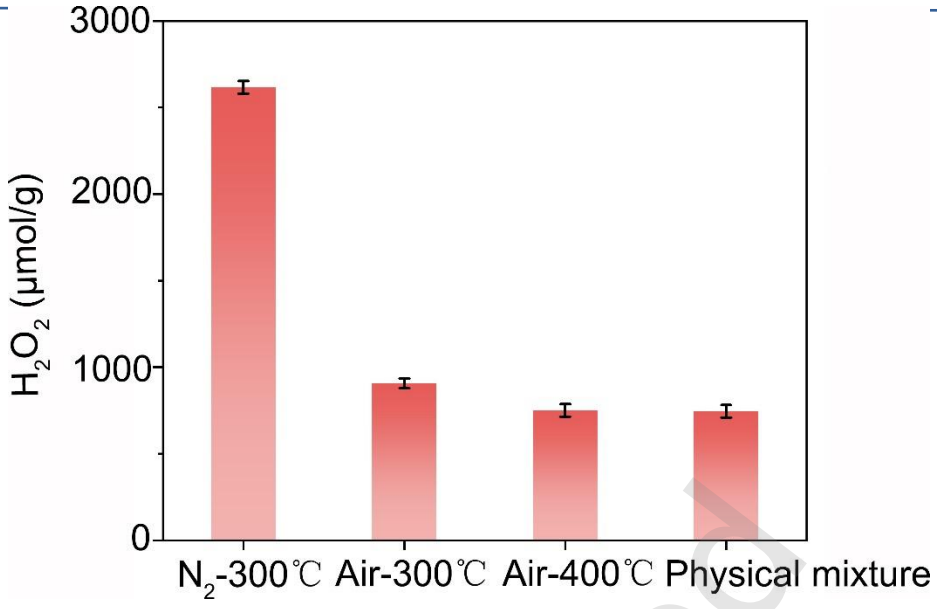


Figure S13. H_2O_2 yields after 150 min of irradiation with a 300 W xenon lamp in pure water under ambient air for In-TCPP@$W_{18}O_{49}$ hybrids prepared using differently treated $W_{18}O_{49}$ supports and a physical mixture of separately prepared In-TCPP and $W_{18}O_{49}$. N_2–300 °C, Air–300 °C, and Air–400 °C denote the atmosphere and temperature used for support treatment. Bars show the mean values, and error bars represent standard deviations from three independent photocatalytic experiments.

Just Accepted

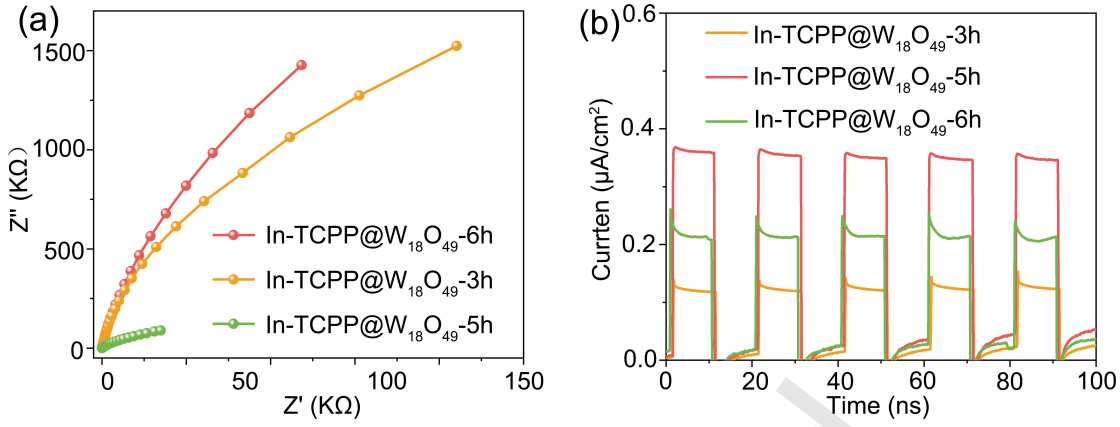


Figure S14. (a) Electrochemical impedance spectra and (b) transient photocurrent responses of In-TCPP@$W_{18}O_{49}$-3h, In-TCPP@$W_{18}O_{49}$-5h, and In-TCPP@$W_{18}O_{49}$-6h.

Just Accepted

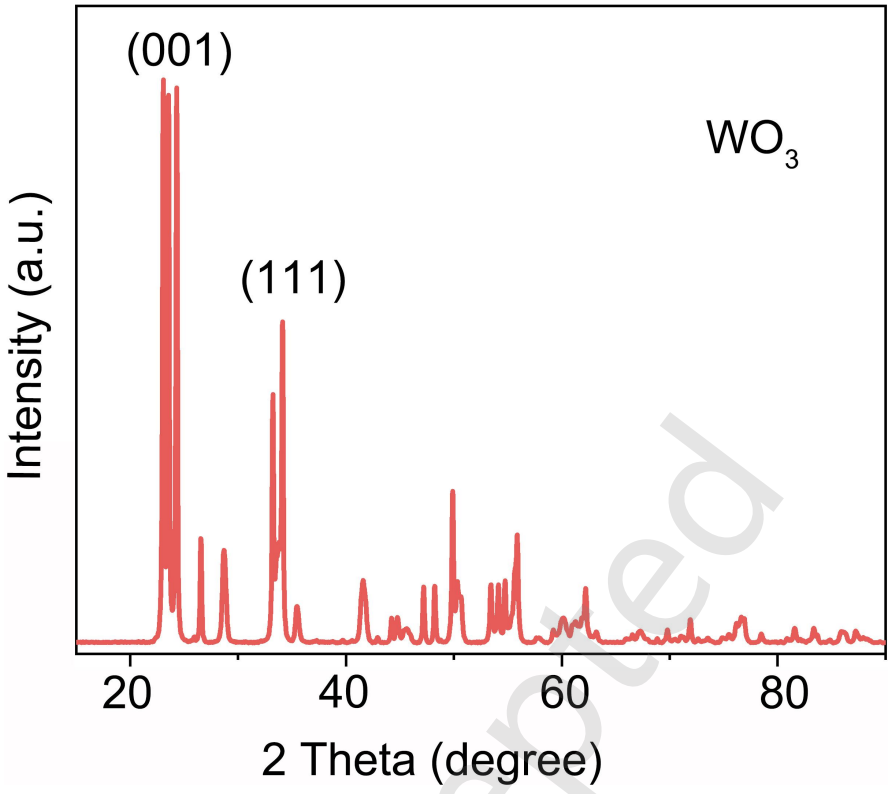


Figure S15. XRD pattern of WO_3.

Just Accepted

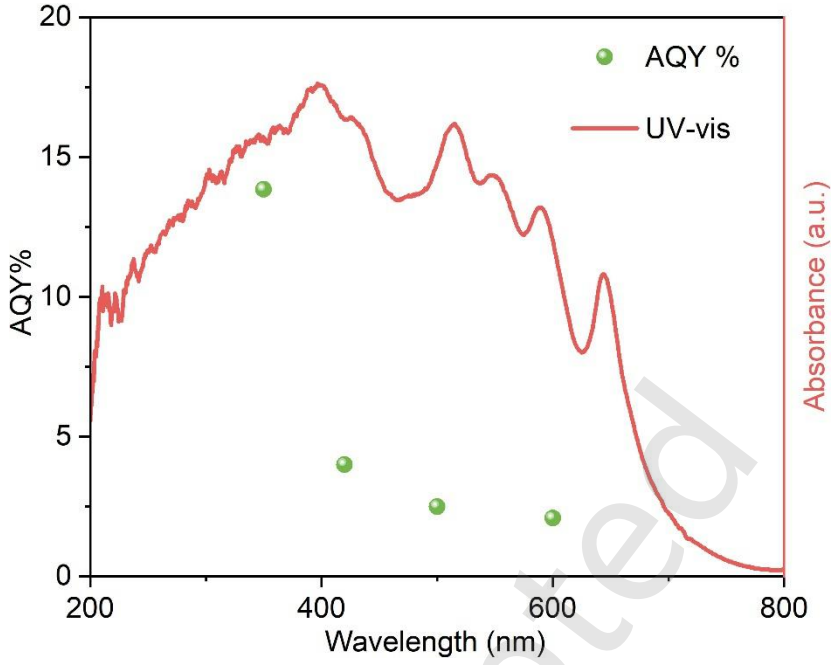


Figure S16. Apparent quantum yields in the presence of benzyl alcohol. Wavelength-dependent apparent quantum yields (AQYs) for H_2O_2 production over In-TCPP@ $W_{18}O_{49}$ in the presence of benzyl alcohol as a sacrificial electron donor, together with the UV–vis absorption spectrum. The catalyst was prepared using 40 mg of $W_{18}O_{49}$ and a solvothermal reaction time of 5 h, corresponding to the optimized sample denoted as In-TCPP@$W_{18}O_{49}$-40 or In-TCPP@$W_{18}O_{49}$-5h.

Just Accepted

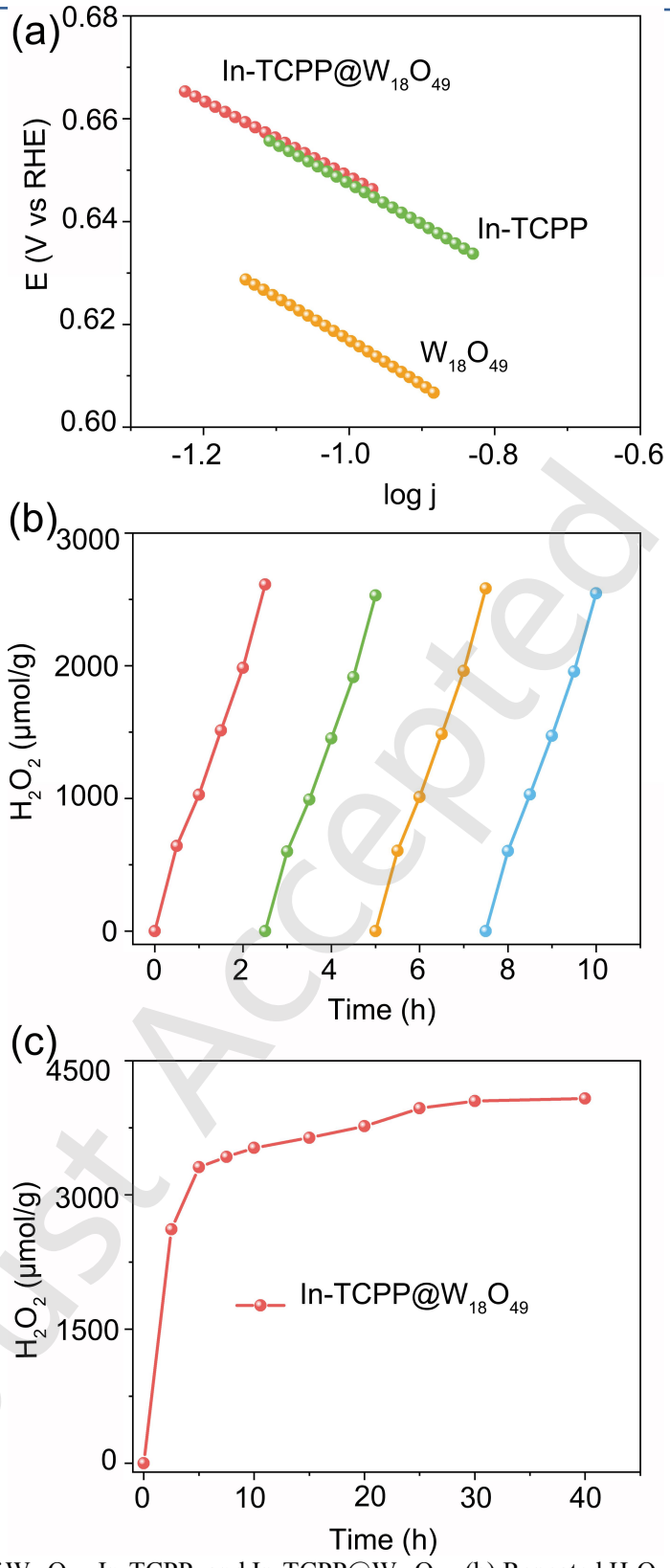


Figure S17. (a) Tafel plots of $W_{18}O_{49}$, In-TCPP, and In-TCPP@$W_{18}O_{49}$. (b) Repeated H_2O_2 production cycles and (c) long-term H_2O_2 accumulation over In-TCPP@$W_{18}O_{49}$.

Just Accepted

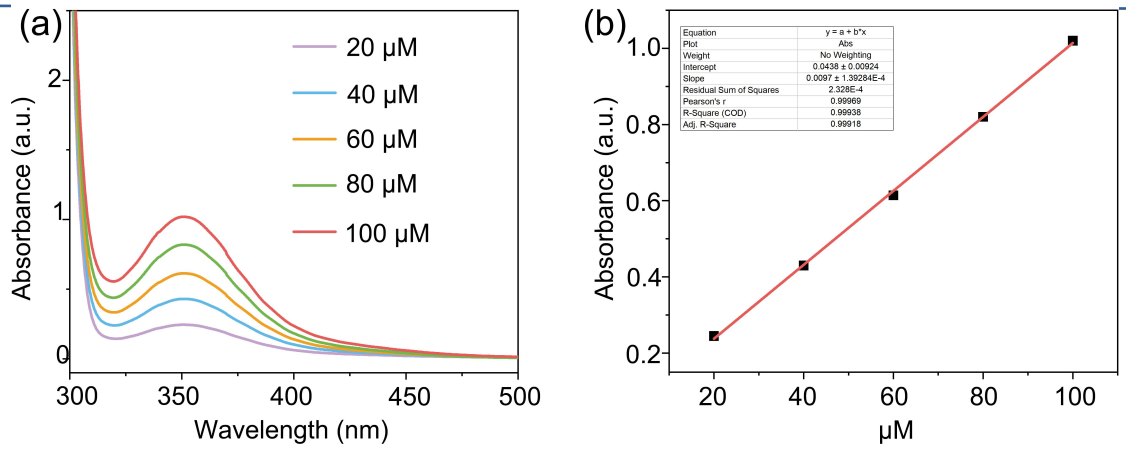


Figure S18. UV–vis calibration for H_2O_2 quantification. (a) UV–vis absorption spectra of standard H_2O_2 solutions with different concentrations. (b) Corresponding calibration curve.

Just Accepted

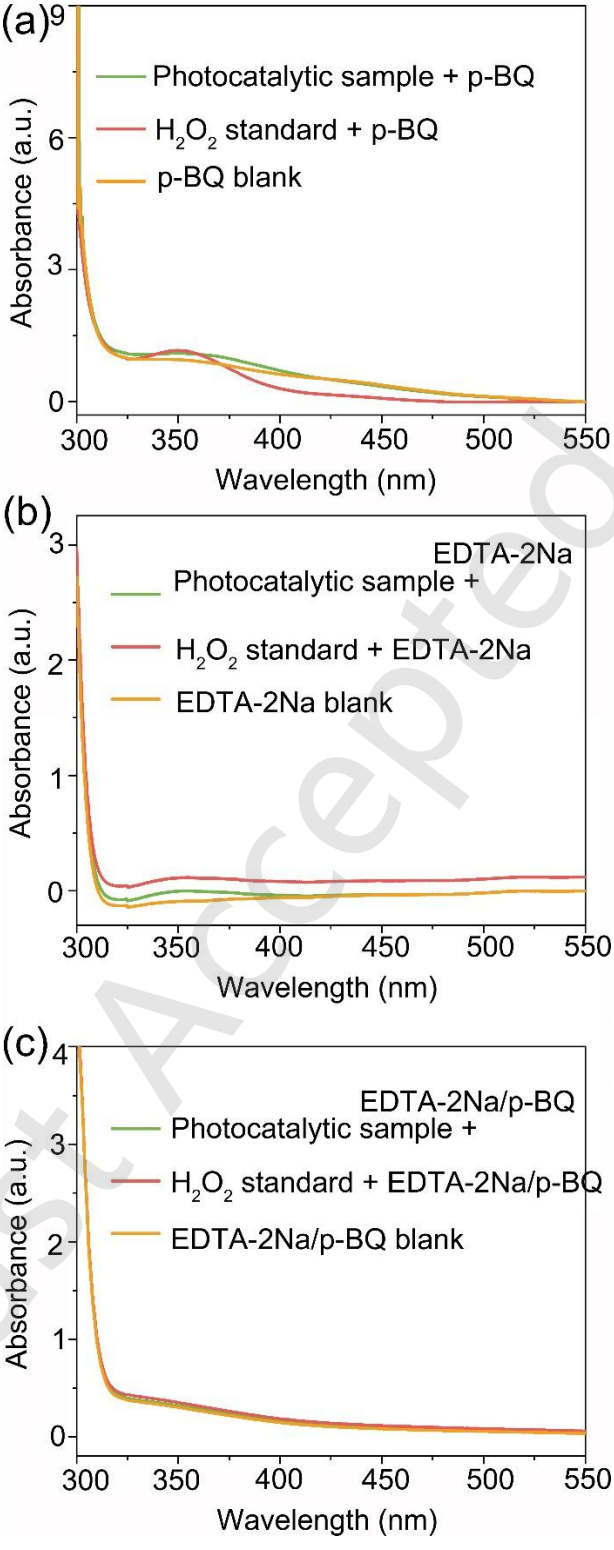


Figure S19. KI-based spectrophotometric measurements in the presence of scavengers. UV–vis spectra after KI color development of photocatalytic reaction supernatants, H_2O_2 standards, and aqueous blanks containing (a) p-BQ, (b) EDTA-2Na, or (c) EDTA-2Na and p-BQ. The reaction supernatants were collected after irradiation of In-TCPP@$W_{18}O_{49}$ suspensions containing the corresponding scavengers.

Just Accepted

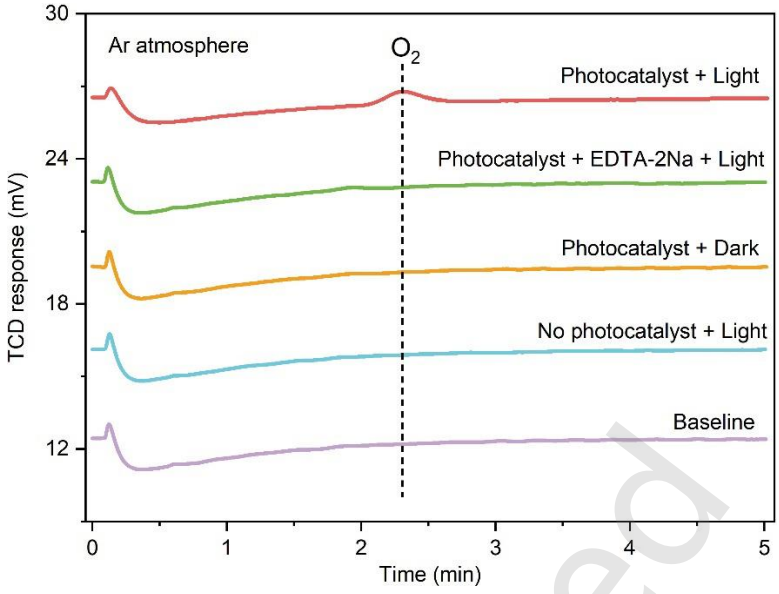


Figure S20. Headspace GC-TCD analysis under an Ar atmosphere. Chromatograms obtained from an aqueous In-TCPP@$W_{18}O_{49}$ suspension under illumination, with EDTA-2Na under illumination, and in the dark, together with water without photocatalyst under illumination and the baseline measurement. The dashed line marks the retention time assigned to O_2. Traces are vertically offset for clarity.

Just Accepted

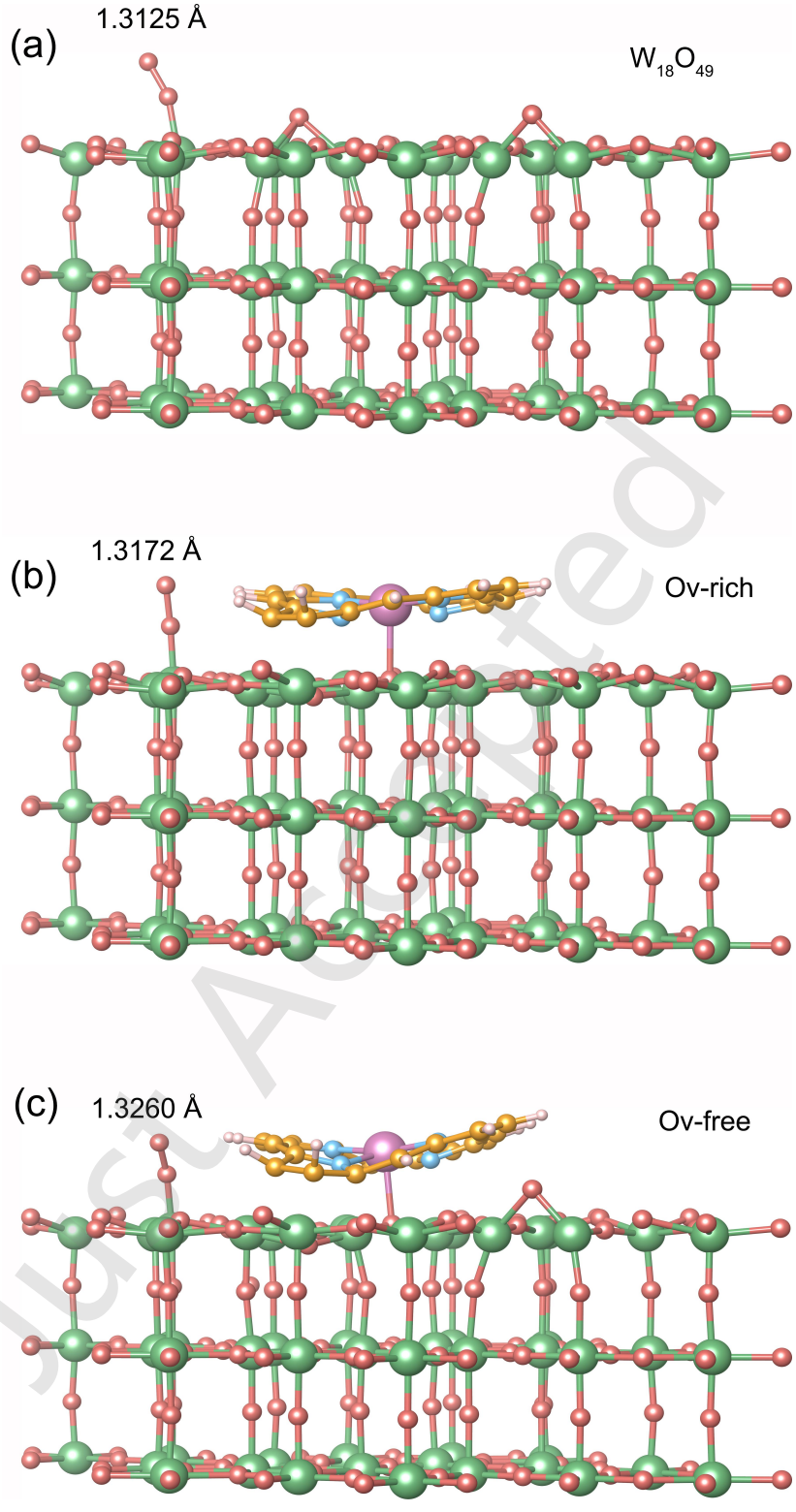


Figure S21. (a) $W_{18}O_{49}$, (b) Ov-free In-TCPP@$W_{18}O_{49}$, and (c) Ov-rich In-TCPP@$W_{18}O_{49}$ interfaces after O_2 adsorption. The corresponding O–O bond lengths are indicated.

Just Accepted

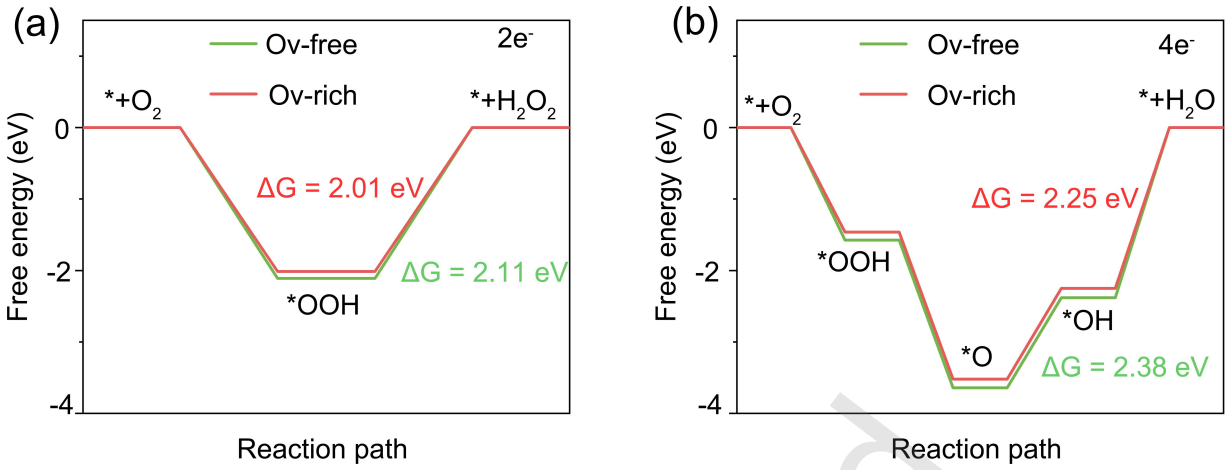


Figure S22. Gibbs free-energy profiles of the competing oxygen reduction pathways on the reference and oxygen-vacancy-rich In-TCPP@$W_{18}O_{49}$ interfaces: (a) the $2e^-$ pathway to H_2O_2 and (b) the $4e^-$ pathway to H_2O. The *OOH to *O step in panel (b) represents O–O bond cleavage.

Just Accepted

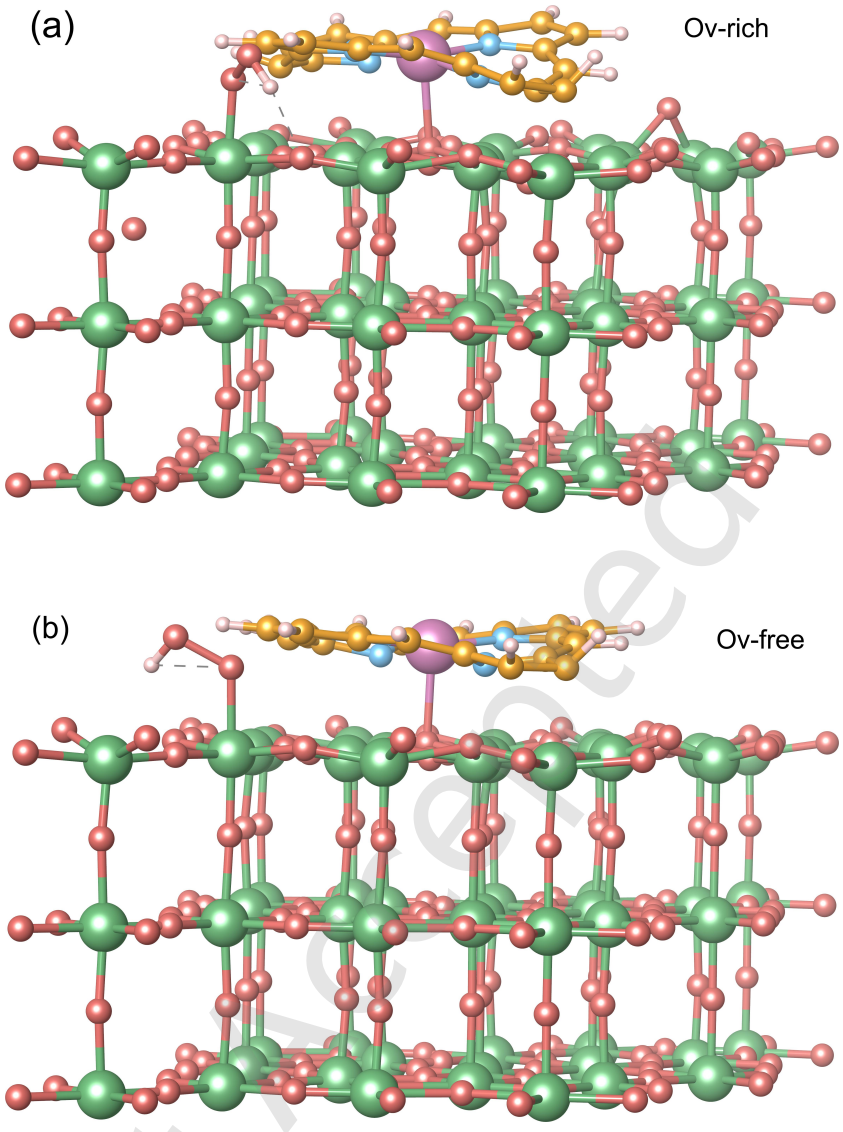


Figure S23. (a) Ov-rich In-TCPP@$W_{18}O_{49}$ and (b) Ov-free In-TCPP@$W_{18}O_{49}$ models after *OOH adsorption.

Just Accepted

Table S1. Photocatalytic H_2O_2 production performance of representative WO_x- and TCPP-based catalysts.

Catalyst	H_2O_2 production rate	Light source	Reaction conditions	Ref.
In-TCPP@$W_{18}O_{49}$	1045 μmol g^{-1} h^{-1}	300 W Xe lamp	Pure water, ambient air	This work
C-$W_{18}O_{49}$/Ni-SA	338.9 μmol g^{-1} h^{-1}	Visible light	Pure water	[1]
Mo-$H_{0.23}WO_{3-x}$	196.25μmol g^{-1} h^{-1}	Visible light	Pure water, O_2	[2]
ZnO/WO_3	6788 μmo L^{-1} h^{-1}	300 W Xe lamp	ethanol, O_2	[3]
Au/WO_3	544 μM	Visible light	methanol, O_2	[4]
Gd-WO_3	0.58 mmo L^{-1} h^{-1}	Visible-light	aqueous pollutant	[5]
WO_3/CdS	1.00 mmol g^{-1} h^{-1}	Visible-light	Seawater	[6]
Ti-MOF/WO_{3-x}	8.41 μmol g^{-1} h^{-1}	300 W Xe lamp	Pure water	[7]
WO_3/Tp-TAPB	1488.4 μmol g^{-1} h^{-1}	Visible-light	Pure water, O_2	[8]
YTU-W-2	345 μmol g^{-1} h^{-1}	Visible light	ethanol, O_2	[9]
In-TCPP/M68N	321.2 μmol g^{-1} h^{-1}	Sunlight	Pure water	[10]
Cu-TCPP/CdSe	2338.23 μmol g^{-1} h^{-1}	Visible light	Pure water	[11]
TCPP-TBAPy	730.45 μmol g^{-1} h^{-1}	Visible light	Pure water	[12]
Al-TCPP-Sb5%	663.2 μmol g^{-1} h^{-1}	Visible light	Pure water	[13]
THF-TCPP	29.33 μmol g^{-1} h^{-1}	300 W Xe lamp	Pure water, O_2	[14]
SA-TCPP	0.66 mM h^{-1}	300 W Xe lamp	Pure water, O_2	[8]
Bi-TCPP	679.79 μmol g^{-1} h^{-1}	455 nm LED	Pure water, O_2	[15]
Ce-TCPP	21.02 μmol g^{-1} h^{-1}	Visible light	Pure water, O_2	[16]
La-TCPP	79.75 μmol g^{-1} h^{-1}	Visible light	Pure water, O_2	[16]

Just Accepted

Table S2. Comparison of H_2O_2 accumulation measured by the KI and Ce(IV) methods in scavenger-containing photocatalytic samples.

Scavenger	KI method ($\mu mol\ g^{-1}$)	Ce(IV) method ($\mu mol\ g^{-1}$)
p-BQ	80.99	83.51
EDTA-2Na	N.D.	N.D.
EDTA-2Na + p-BQ	N.D.	N.D.

Just Accepted

References

[1] Jin, C.; Shen, H.; Li, J.; Guo, X.; Rao, S.; Yang, W.; Liu, Q.; Sun, Z.; Yang, J. Isolated ni atoms for enhanced photocatalytic H_2O_2 performance with 1.05% solar-to-chemical conversion efficiency in pure water. *Nano Lett.*, 2024, **24**, 14484–14492.

[2] An, K.; Wu, B.; Hu, J.; Bai, X.; Wang, P.; Fang, Y.; Jiang, R.; Wang, J. Schottky‐barrier‐free plasmonic WO_3‐based photocatalysts for simultaneous N_2 fixation and H_2O_2 generation. *Advanced Materials*, 2026, **38**, e15476.

[3] Jiang, Z.; Cheng, B.; Zhang, Y.; Wageh, S.; Al‐Ghamdi, A. A.; Yu, J.; Wang, L. S-scheme ZnO/WO_3 heterojunction photocatalyst for efficient H_2O_2 production. *Journal of Materials Science & Technology*, 2022, **124**, 193–201.

[4] Wang, Y.; Wang Y.; Zhao J.; Chen M.; Huang X.; Xu Y. Efficient Production of H_2O_2 on Au/WO_3 under Visible Light and the Influencing Factors. *Appl. Catal. B Environ*. 2021, **284**, 119691..

[5] Wang, J.; Wang, J.; Zuo, S.; Pei, J.; Liu, W.; Wang, J. Cooperative coupling of photocatalytic production of H_2O_2 and oxidation of organic pollutants over gadolinium ion doped WO_3 nanocomposite. *Chinese Chemical Letters*, 2023, **34**, 108157.

[6] Wang, Y.-N.; Guo, Y.; Peng, J.; Zhao, J.; Yang, L.; Song, H.; Chen, C. Construction of spherical WO3/CdS S-scheme heterojunction for photocatalytic H2O2 production in real seawater. *Journal of Environmental Chemical Engineering*, 2025, **13**, 115296.

[7] Jiang, H.; Wang, L.; Yu, X.; Sun, L.; Li, J.; Yang, J.; Liu, Q. Precise regulation of built-in electric field over NH_2-MIL-125-T/WO_{3-x} S-scheme heterojunction for achieving simultaneous formation of CO and H_2O_2 from CO_2 and H_2O. *Chemical Engineering Journal*, 2023, **466**, 143129.

[8] Rasaily, S.; K. Dam, G.; Ghosh, S. K. Advanced Functional Porous Materials for Photocatalytic H_2O_2 Production. *Chem. Sci.* 2026, **17**, 13296–13343..

[9] Wang, X.; Li, J.; Wei, X.; Song, J.; Xie, J.; Li, Z.; Yuan, M.; Jiang, L.; Wang, Y.; Liang, C.; Liu, W. Photocatalytic hydrogen peroxide production by a mixed ligand-functionalized uranyl–organic framework. *ACS Omega*, 2024, **9**, 33671–33678.

[10] Cai, Z.; Liu, H.; Dai, J.; Li, B.; Yang, L.; Wang, J.; Zhu, H. Sunlight-driven simultaneous CO_2 reduction and water oxidation using indium-organic framework heterostructures. *Nat Commun*, 2025, **16**, 2601.

[11] Bian, Y.; Wang, Z.; Du, M.; Dai, K.; Yu, J.; Zhang, L. Strain‐amplified interfacial electric field in an S‐scheme cu‐TCPP/CdSe heterojunction for efficient photocatalytic H_2O_2 production in pure water. *Adv Funct Materials*, 2026, **36**, e19493.

[12] Wang, N.; Wang, X.-F.; Bao, C.-H.; Liu, Y.-T.; Jin, C.-C.; Ding, K.; Li, L.; Wang, X.; Chen, Z. Efficient H_2O_2 photosynthesis in pure water enabled by multivariate hydrogen-bonded organic framework. *Journal of Colloid and Interface Science*, 2026, **721**, 140759.

[13] Li, L.; Wang, X.-F.; Bao, C.-H.; Wang, X.; Jin, C.-C.; Wu, J.; Chen, Z.; Yamauchi, Y.; Ok, Y. S. Implanting single sb sites as electron traps on MOF nanosheets for boosting H_2O_2 photosynthesis. *Applied Catalysis B: Environment and Energy*, 2026, **388**, 126555.

[14] Shao, Y.; Zhang, Y.; Chen, C.; Dou, S.; Lou, Y.; Dong, Y.; Zhu, Y.; Pan, C. Enhancement of H_2O_2 generation rate in porphyrin photocatalysts via crystal facets regulation to create strong internal electric field. *Chinese Journal of Catalysis*, 2024, **61**, 205–214.

[15] He, L.; Chen, E.-X.; Xiang, J.-Q.; Guo, Y.-J.; Zhang, J.; Lin, Q. Mesoscopic spiral nanoplates formed by porphyrin-spaced coordination frameworks for enhanced H_2 O_2 photosynthesis. *Inorg. Chem. Front.*, 2024, **11**, 8037–8046.

[16] Naveen T.; Anchal P.; Vatika S.; Pankaj Ra.; Pardeep S.; Aftab A.; Van-Huy N.; Chinh C.; Seok J.; Quyet V.; Hyojung K.; Sonu S. Next-generation wastewater treatment with emerging 2D MOF-derived photocatalysts. *ACS omega* 2025, **10**, 58029–58056.

Just Accepted

Address correspondence to First A. Firstauthor, email1; Third C. Thirdauthor, email2